iScience

CellPress
OPEN ACCESS

Article

C-Mannosylation Enhances the Structural Stability of Human RNase 2

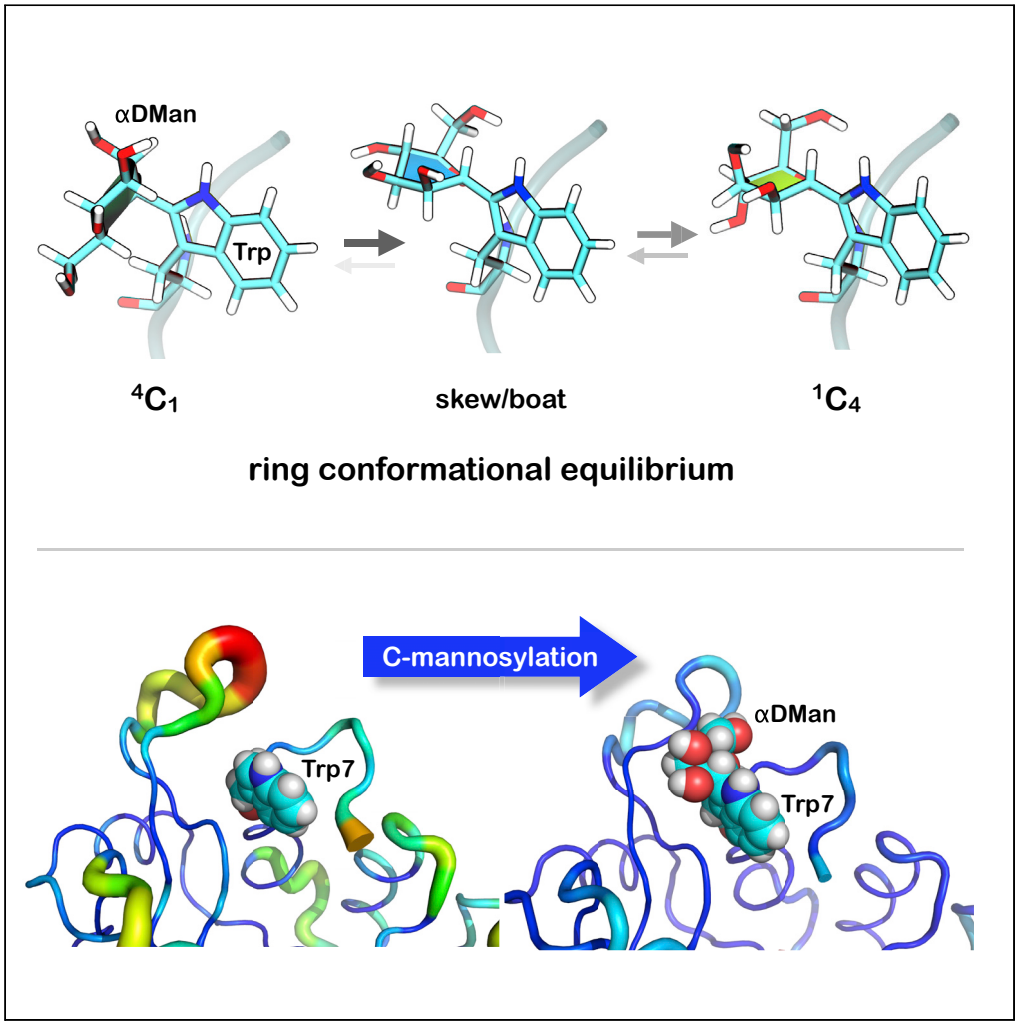

Martin Frank, Daniela Beccati, Bas R. Leeflang, Johannes F.G. Vliegenthart

j.f.g.vliegenthart@uu.nl

HIGHLIGHTS

NMR and MD show that C-linked mannose exists as an ensemble of conformations

Conformation of mannose is influenced by the protein environment and solvent

In RNase 2 mannose favors a conformation that optimally stabilizes the protein fold

Efficient methods for analysis of a large number of MD trajectories are presented

Frank et al., iScience 23, 101371
August 21, 2020
https://doi.org/10.1016/j.isci.2020.101371

iScience

CellPress
OPEN ACCESS

Article

C-Mannosylation Enhances the Structural Stability of Human RNase 2

Martin Frank,[2] Daniela Beccati,[1,3] Bas R. Leeflang,[1,4] and Johannes F.G. Vliegenthart[1,5,*]

SUMMARY

C-Mannosylation is a relatively rare form of protein glycosylation involving the attachment of an α-mannopyranosyl residue to C-2 of the indole moiety of the amino acid tryptophan. This type of linkage was initially discovered in RNase 2 from human urine but later confirmed to be present in many other important proteins. Based on NMR experiments and extensive molecular dynamics simulations on the hundred microsecond timescale we demonstrate that, for isolated glycopeptides and denatured RNase 2, the C-linked mannopyranosyl residue exists as an ensemble of conformations, among which $^{1}C_{4}$ is the most abundant. However, for native RNase 2, molecular dynamics and NMR studies revealed that the mannopyranosyl residue favors a specific conformation, which optimally stabilizes the protein fold through a network of hydrogen bonds and which leads to a significant reduction of the protein dynamics on the microsecond timescale. Our findings contribute to the understanding of the biological role of C-mannosylation.

INTRODUCTION

Glycosylation is one of the most common posttranslational modification of proteins, and the best known types are N- and O-glycosylation (Spiro, 2002). In the 1990s, C-glycosylation was discovered in human ribonuclease (RNase) 2, where an α-D-mannopyranosyl residue was attached to the C2 atom of the indole ring of Trp7 via a carbon-carbon bond (Hofsteenge et al., 1994; De Beer et al., 1995). In 1998, Krieg et al. proposed on the basis of site-directed mutagenesis the sequence Trp-X-X-Trp as the recognition motif for *C*-mannosylation, in which the Trp residue positioned toward the N terminus becomes mannosylated. It was later demonstrated that in thrombospondin type 1 repeats the second Trp residue is not essential for *C*-mannosylation (Gonzalez de Peredo et al., 2002) and can be replaced by Cys (Julenius, 2007).

C-mannosylation has been experimentally verified in approximately seventy glycosylation sites (Ihara et al., 2015) of proteins such as interleukin-12 (Yoon et al., 2000), the terminal four components of human complement system C6, C7, C8, and C9 (Hofsteenge et al., 1999), human platelet thrombospondin-1 (Hofsteenge et al., 2001), properdin (Hartmann and Hofsteenge, 2000), recombinant erythropoietin receptors (Furmanek et al., 2003), mucins MUC5AC and MUC5B (Perez-Vilar et al., 2004), MAG (Pronker et al., 2016), and hyaluronidase 1 (Goto et al., 2014). Screening of the human genome yielded about 2,600 exported or trans-membrane transcripts with at least one predicted *C*-Man site (Julenius, 2007), indicating that *C*-mannosylation is a more important protein modification than initially thought. It is now acknowledged that *C*-mannosylation is not limited to mammalian proteins but is present in the glycoprotein of the Ebola virus (Falzarano et al., 2007) and in the hypertrehalosemic hormone from the stick insect *Carausius morosus* (Munte et al., 2008).

C-mannosylation is a posttranslational modification that occurs intracellularly in the endoplasmic reticulum before protein folding and secretion (Krieg et al. 1997, 1998; Doucey et al., 1998) by a microsomal transferase previously isolated and characterized (Hamann et al., 1989). Its biological significance has not been unambiguously elucidated yet. It is believed that, when the polar mannose attaches to the non-polar tryptophan it affects the protein polarity, probably inducing a conformational change that affects protein functions such as protein stability, secretion, intracellular localization, and enzymatic activity (Goto et al., 2014).

Although direct involvement of *C*-mannose in adhesion phenomena of the W-X-X-W motif of thrombospondin type 1 repeat (TSR) modules is still being debated, Ihara et al. (2010) demonstrated, with the

[1]Bijvoet Center, Division of Bio-Organic Chemistry, Utrecht University, Padualaan 8, Utrecht 3584 CH, The Netherlands

[2]Biognos AB, Box 8963, Göteborg 40274, Sweden

[3]Present address: Shiseido Americas Corporation, One Kendall Square, Cambridge, MA 02139

[4]Present address: Geosciences, Utrecht University, Princetonlaan 8a, Utrecht 3584CB

[5]Lead Contact

*Correspondence: j.f.g.vliegenthart@uu.nl

https://doi.org/10.1016/j.isci.2020.101371

use of synthesized *C*-Man-WSPW and WSPW peptides, that in RAW264.7 cells some proteins specifically recognized *C*-Man-WSPW but not WSPW. Among these, the shock cognate protein 70 (Hsc70) had higher affinity in solution to *C*-mannosylated peptides compared with non-mannosylated ones. A study by Li et al. (2009) shows that *C*-mannosylated mindin from HEK 293 cells binds LPS through its TSR domain, whereas the bacterially expressed mindin that lacks *C*-mannose does not recognize LPS. Ihara et al. (2005) reported increased expression of *C*-mannosylation in the aortic vessels of diabetic Zucker rats, suggesting a pathological role for the increased *C*-mannosylation in the development of diabetic complications. Several studies demonstrated the biological importance of *C*-mannosylated tryptophan, although they could not investigate the contribution played by the *C*-mannose without modifying the target protein sequence. Otani et al. (2018) demonstrated that *C*-mannosylated tryptophan in G-CSFR plays a role in myeloid cell differentiation through regulation of downstream signaling. Sasazawa et al. (2015) showed how *C*-mannosylated tryptophan residues of the thrombopoietin receptor (c-Mpl) regulates thrombopoietin-dependent JAK-STAT signaling. Okamoto et al., 2017 revealed that mutagenesis of the *C*-mannosylation site reduced both secretion efficiency and enzymatic activity of *C*-mannosylation-defective mutant lipoprotein lipase-overexpressing cell lines compared with the wild-type. The identification of the gene encoding *C*-mannosyltransferase (Buettner et al., 2013), the enzyme affecting *C*-mannosylation, enabled genetic interventions aimed at modulating *C*-mannosylation without affecting target protein sequences and allowed studies that provided direct evidence for the specific role of *C*-mannosylation in the secretion of proteins containing TSR motif (Niwa et al., 2016; Shcherbakova et al., 2017).

The impact of *C*-mannosylation on the three-dimensional structure of proteins is not very well understood. Several studies have suggested changes in protein conformations due to the presence of *C*-mannose. Using NMR, Hinou et al., 2016 analyzed peptides synthesized to mimic the WSXWS motif of the erythropoietin receptor (EPOR) and compared them with the corresponding synthetic peptides lacking the *C*-mannose residue. Through analysis of NOEs signals, they were able to show that *C*-mannosylation works as a stabilizer of the WSXWS motif and the neighbor aryl side chain. Hartmann and Hofsteenge (2000) hypothesize that the 14 mannose residues linked to properdin are exposed at the surface of the protein in virtue of their hydrophilic character and mediate properdin interaction with the multivalent mannose-binding lectin present in serum. Tan et al. (2002) showed that the occurrence of several (C^2-α-D-Man-)Trp residues in TSR modules poses steric constraints on the protein conformation. The polypeptide chain cannot adopt a helical conformation, and the mannosylated Trp residues are oriented so that their polar atoms are exposed and available for potential ligand binding. For MUC5AC and MUC5B (Perez-Vilar et al., 2004), ADAMTS-like 1 (Wang et al., 2009), and UNC5A (Shcherbakova et al., 2017) *C*-mannosylation is required for proper folding or subsequent endoplasmic reticulum exit. In TSR modules the *C*-mannosylated tryptophans are part of a 3D structural motif called "Trp-Arg ladder," where up to three tryptophans (building a WxxWxxW motif) from one strand are stacked with conserved arginine residues (RxRxR motif) from a second strand. Such an arrangement of amino acid side chains is most likely stabilized by cation-π interactions. For properdin it has been shown by X-ray crystallography that the mannose can form hydrogen bonds with an adjacent arginine, which further stabilizes the Trp-Arg ladder (Pedersen et al., 2019). Such a stabilization has been recently confirmed experimentally for thrombospondin type 1 repeats of netrin receptor UNC-5 (Shcherbakova et al., 2019). However, it should be noted that a Trp-Arg ladder motif is not present in RNase 2.

Following the initial discovery of *C*-mannosylation in RNase 2, extensive studies were conducted to identify the conformation of the C^2-α-D-mannopyranosyl-L-tryptophan moiety (De Beer et al., 1995; Löffler et al., 1996). Since then, the X-ray structures of a number of *C*-mannosylated proteins have been determined; for example, interleukin-21 receptor bound to IL-21 (Hamming et al., 2012), interleukin-2 receptor (Klein et al., 2017), human complement system C6 (Aleshin et al., 2012), C5b6 (Hadders et al., 2012), C8 (Lovelace et al., 2011), MAG (Pronker et al., 2016), and properdin (van den Bos et al., 2019) (for a full list of available X-ray structures see Table S1). However, the electron density of the C-linked mannoses is frequently not sufficient to unambiguously determine their conformation (compare structures in Figure 1). Consequently, despite the availability of several X-ray structures, many structural aspects of the conformation of the α-D-Man*p*-Trp moiety remain unclear.

NMR spectroscopy revealed that the pyranose ring is not rigid in the hexapeptide FTW^{Man}AQW isolated from RNase 2 (De Beer et al., 1995; Löffler et al., 1996) and adopts several conformations on the NMR timescale. Although there are some indications that the $^1C_4$ conformation is the most prominent conformation in the ensemble, the other conformations present are unknown. Additionally, it has been shown that in human RNase 2 the orientation around the C-linkage occupied by the mannose residue in the native protein is

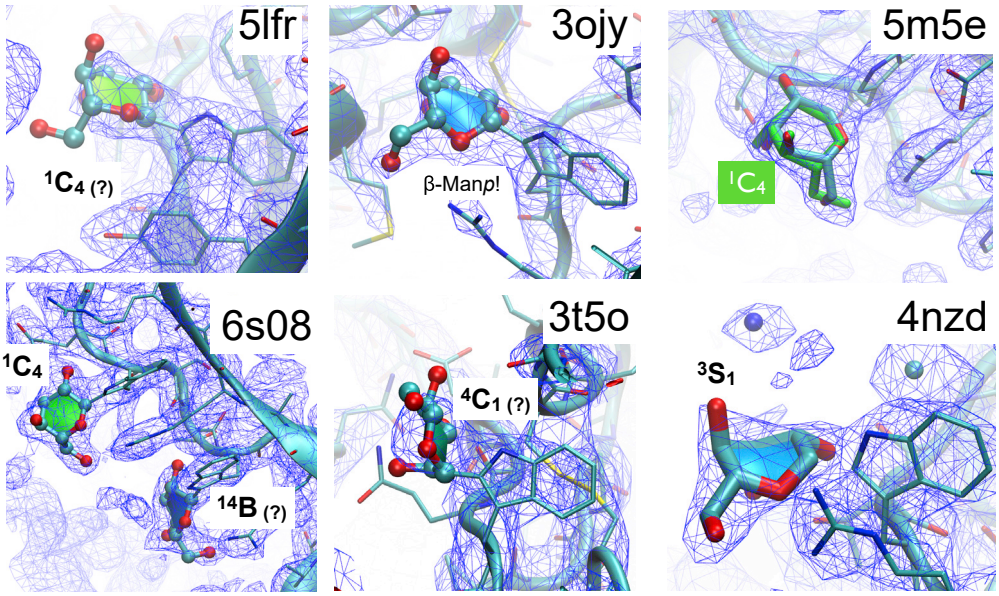

Figure 1. Examples of X-ray Crystal Structures Containing the α-D-Man*p*-Trp Moiety

Well-resolved electron density supporting a $^1C_4$ conformation of mannose is present in PDB entry 6s08 and 5m5e. Please note that in general the modeled ring shapes of carbohydrates in PDB structures should be taken with care (Agirre et al., 2017). As an example, PDB entry 5m5e is shown with a re-modeled mannose (shown in green) in $^1C_4$ conformation, which fits at least equally well into the electron density than the distorted ring shape modeled in the original X-ray structure published. In most X-ray structures listed in Table S1 the electron density around the C-linked mannoses is not well resolved or the conformation of the mannose is ambiguous (indicated with a "?"). PDB entry 3ojy has β-D-Man*p* covalently attached to Trp, which is most likely not correct. The electron density in PDB entry 4nzd may support the existence of twisted ring shapes (skew, boat) of C-linked mannose. See also Table S1.

different from that in the denatured form. The objective of the present study was to explore the conformation of the C-linked α-mannose by molecular modeling and to determine how the usual pyranose $^4C_1$ conformation of the mannose residue may be destabilized in favor of the $^1C_4$ conformation. To gain insight into the possible influence of the polypeptide chain on the conformation of the C-linked α-D-mannopyranosyl moiety, further NMR studies were carried out on glycopeptides of different chain length and amino acid composition.

NMR, molecular modeling, and molecular dynamics (MD) studies were performed on ManTrp, *C*-Man containing peptides, and both native and denatured RNase 2. Importantly, we investigated in which way the three-dimensional structure of RNase 2 could be responsible for the different orientation of *C*-mannose in native and denatured protein. Since RNase has the same amino acid sequence as eosinophil-derived neurotoxin (EDN) (Hamann et al., 1989), the three-dimensional structure of recombinant EDN (rEDN from *Escherichia coli*), as determined by X-ray crystallography (Mosimann et al., 1996; Swaminathan et al., 2002), was used to model the C-linkage between mannose and Trp. The short distances between the neighboring amino acid protons and those of the α-D-mannopyranosyl residue, as observed by molecular modeling, were finally compared with the NMR data on native RNase 2. Our results show that in native RNase 2 the mannopyranosyl residue favors a specific conformation, which optimally stabilizes the protein fold through a network of hydrogen bonds and which leads to a significant reduction of the protein dynamics.

RESULTS

Structural Analysis of C^2-α-D-Mannopyranosyl-L-Tryptophan by NMR in Peptides Isolated from Human RNase 2

The structure and atom designation of C^2-α-D-mannopyranosyl-L-tryptophan is presented in Figure 2. The complete NMR assignment of this moiety was first obtained from analysis of the *C*-glycopeptide FTW^{Man}AQW isolated from human RNase 2 (Hofsteenge et al., 1994) and was later on confirmed by analysis of the (C^2-α-D-Man-) Trp compound generated by total synthesis (Manabe and Ito, 1999). Previous studies indicate that the *C*-

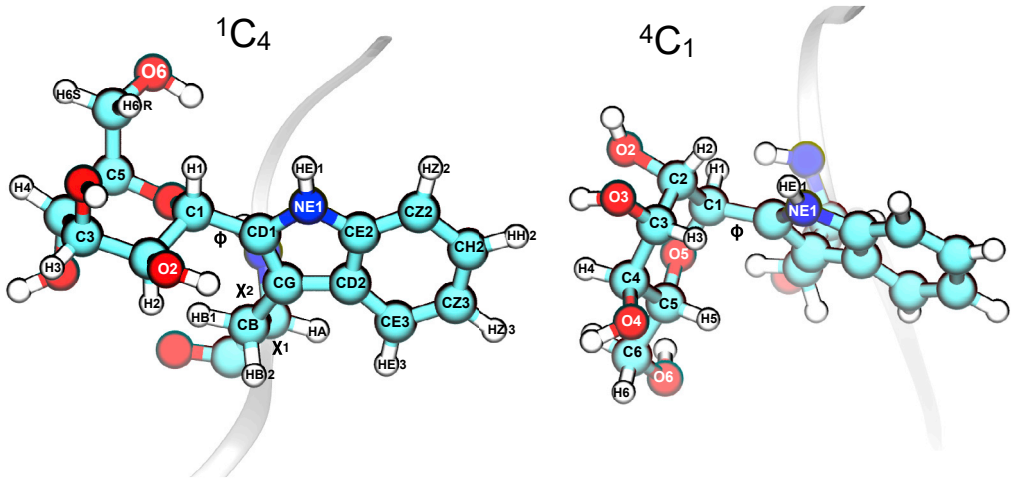

Figure 2. C^2-α-D-mannopyranosyl-L-tryptophan Moiety

3D representations of two chair conformations: $^1C_4$ (left), $^4C_1$ (right). The peptide backbone is indicated as ribbon. Selected atom and torsion labels are shown. For definitions of torsion angles see Supplemental Information, Molecular Modeling section.

α-mannopyranosyl residue must exist in an ensemble of conformations on the NMR timescale (De Beer et al., 1995), among which the most represented is the $^1C_4$ chair conformation with an equatorially oriented tryptophan moiety (Manabe and Ito, 1999).

To determine whether the (C^2-α-D-Man-)Trp conformation could be influenced by the presence of neighboring amino acids, or whether the presence of the C-linked mannose could reduce the flexibility of the amino acid region linked to it, peptides with different chain length were here isolated from human RNase 2 and characterized by ^{1}H NMR (Table 1). Chemical shifts and coupling constants of the (C^2-α-D-Man-)Trp in the RNase 2 peptides were also compared with values for the chymotryptic peptide SSSW^{Man}SEW isolated from human interleukin-12 (Doucey et al., 1999) and the tryptic peptide MSPW^{Man}SEWSQCDPCLR isolated from the terminal component C9 of the human complement system (Hofsteenge et al., 1999). Although the reported fragments present different amino acid sequences, they closely resemble each other with respect to chemical shifts and coupling constants of the (C^2-α-D-Man-)Trp moiety, indicating a similar conformation of the mannose ring. In all the reported peptides, Man $^3J_{1,2}$ couplings constants present values around 7–8 Hz that are incompatible with the usually preferred $^4C_1$ conformation of aldohexopyranoses and preclude all conformations with a small H1/H2 coupling constant ($^4C_1$, $^{0,3}B$, $B_{0,3}$, $B_{1,4}$, $^{2,5}B$, $^3S_1$, $^5S_1$, $^2S_0$, see Table S2).

Rotating-frame Overhauser Effect (ROE) analysis of the RNase peptides reveals no signals between H1 and H4 of the mannosyl residue, which excludes all the conformations presenting a short distance between H1 and H4 ($^{1,4}B$, $^1S_5$, and $^1S_3$) (see Table S3). The strong ROE signal between H1 and H6 allows elimination of conformations with a long distance between these two protons, i.e., $B_{2,5}$ and $^0S_2$, and indicates that the hydroxymethyl group is not in its preferred equatorial position.

The best agreement with the experimental ROE data is obtained for the $^1C_4$ chair conformation, which has a predicted $J_{3,4}$ value of 2.8 Hz. However, this is significantly different from the experimental $J_{3,4}$ value of 5.3 Hz (see Table S3); therefore the data presented here are not in agreement with a single conformation of the mannose. Consequently, the C-linked mannopyranosyl residue most likely exists in an ensemble of conformations, among which $^1C_4$ seems to be the most populated. It could be argued that the normally preferred $^4C_1$ conformation may not be stable owing to the preference of the rigid Trp ring to adopt an equatorial position that minimizes steric interactions and forces the hydroxymethyl group out of its preferred equatorial position (De Beer et al., 1995). It should be noted that the J-couplings of the mannosyl residue do not match one single conformation; therefore, the mannose ring is supposed to maintain some dynamics in all these peptides. ROE spectra of RNase 2 peptides show no signals between the *C*-mannopyranosyl residue and the neighboring amino acid side chains, and no evidence of long-range

	W_{Man}[a]		$W^{Man}AQW$[a]		$FTW^{Man}AQW$[a,b]		$SSSW^{Man}SEW$[c]		$MSPW^{Man}SEW$[d]
	δ_H	$J_{i,i+1}$	δ_H	$J_{i,i+1}$	δ_H	$J_{i,i+1}$	δ_H	$J_{i,i+1}$	δ_H
Man H1	5.17	8.2	5.14	8.2	5.22	7.8	5.18	7.5	5.18
Man H2	4.42	3.2	4.40	3.1	4.42	3.2	4.44	3.0	4.44
Man H3	4.11	5.3	4.08	5.4	4.09	5.5	4.07	9.1[e]	4.07
Man H4	3.95	3.4	3.94	3.8	3.96	3.8	3.93		3.94
Man H5	3.89	8.7	3.84	8.2	3.87	8.3/3.3	3.83	8.3/3.4	3.82
Man H6S	4.25		4.18		4.21		4.18		4.18
Man H6R	3.73		3.75		3.77		–		–
Trp HE3 (H4)	7.65		7.57		7.67		7.65		7.53
Trp HZ3 (H5)	7.13		7.12		7.14		7.14		7.11
Trp HH2 (H6)	7.22		7.21		7.20		7.20		7.20
Trp HZ2 (H7)	7.44		7.44		7.41		7.42		7.42

Table 1. ^{1}H Chemical Shifts δ_H (ppm) and Homonuclear Vicinal ^{1}H–^{1}H Coupling Constants $J_{i,i+1}$ (Hz) of the *C*-Glycosylated Amino Acid Residues in Isolated Peptides, Measured at 300 K

See also Tables S2 and S7.

[a]Digested peptides from human RNase 2.

[b]Values match the ones previously reported by Hofsteenge et al. (1994).

[c]The 316β–322β chymotryptic peptide from human interleukin-12. Values taken from Doucey et al. (1999).

[d]The 24–38 tryptic peptide ($MSPW^{Man}$SEWSQCDPCLR) from C9 of human complement system. Values taken from Hofsteenge et al. (1999).

[e]$J_{3'4'}+J_{4'5'}$.

connectivities between amino acids or secondary structure, arguing against a significant stabilization of the analyzed peptides. These findings agree with data previously reported for the $MSPW^{Man}$SEWSQCDPCLR fragment, which has no defined structure and presents *J* couplings typical of random coils (Hofsteenge et al., 1999). In conclusion, all the investigated peptides are presumably disordered, and their primary structure does not influence the conformation of the (C^2-α-D-Man-)Trp moiety.

NMR Studies of *C*-Mannose in Native and Denatured RNase 2

Previously, NMR measurements on RNase 2 showed that the mannose residue adopts different orientations around its C-linkage in the native and denatured protein (Löffler et al., 1996). In the native protein, Man H1 is closer to Trp HE1 (Löffler et al., 1996). However, in the denatured protein rotation around the Trp-Man bond brings Man H1 close to Trp HB1/HB2 and Trp HA, analogously to what was detected for the peptides isolated from RNase 2 (Löffler et al., 1996; De Beer et al., 1995) (see Table 2). The three-dimensional structure of native RNase 2 seems to induce a specific orientation of the mannose residue.

Analysis of TOCSY (Total Correlation Spectroscopy) and NOESY (Nuclear Overhauser Effect Spectroscopy) experiments of native and denatured RNase allowed assignment of ^{1}H chemical shifts for the *C*-mannopyranosyl residue (see Table 3). Values for the denatured protein are close to the ones reported for the digested peptides (see Table 1), whereas the native protein differs significantly for the chemical shifts of H2 and H6S. It can therefore be concluded that the three-dimensional structure of the protein affects the conformational features of the *C*-mannopyranosyl residue, probably through long-range connectivities. In fact, NOE signals identified interactions between Man H2-Val128(Me) and between Man H3 and HB2 of an Asp residue, which could not be undoubtedly attributed to either Asp112 or Asp115 due to overlap of NMR signals that prevented full protein assignment.

Conformational Analysis of Model Compounds and Glycopeptides

In order to gain a detailed insight into the conformational preferences of the C^2-α-D-mannopyranosyl-L-tryptophan moiety (compare Figure 2) a variety of model systems with increasing complexity were studied. First, we used C^2-α-D-mannopyranosyl-3-methyl-indole as a basic model compound to investigate the

	Native	Denatured/Isolated Peptides
Man H3–Man H5		[a]Weak, reported by De Beer et al. (1995)
Man H1–Man H6		[a]Strong, reported by De Beer et al., (1995) [b]Reported by Löffler et al. (1996)
Man H4–Man H6		[a]Medium, reported by De Beer et al. (1995)
Man H2–Man H3		[a]Strong, reported by De Beer et al. (1995)
Man H1–Trp HE1	Reported by Löffler et al. (1996)	
Man H1–Trp HA		[a]Reported by De Beer et al. (1995) [b]Reported by Löffler et al. (1996)
Man H1–Trp HB1/HB2		[a]Reported by Hofsteenge et al. (1994) [b]Reported by Löffler et al. (1996)
Man H2–Trp HE1		[a]Reported by Hofsteenge et al. (1994)
Man H2–Trp HB1/HB2	Reported by Löffler et al. (1996)	[b]Reported by Löffler et al. (1996)
Man H6–Trp HE1	Reported by Löffler et al. (1996)	
Man H2-Val128(Me)	Reported by Vliegenthart and Casset (1998)	

Table 2. ROEs/NOEs Observed *C*-Mannopyranosyl Moiety in Native and Denatured RNase 2
See also Table S3.
[a]Isolated peptide.
[b]Denatured Protein.

correlation between ring shape and preferred orientation of the *C*-glycosidic torsion ϕ_H (H1-C1-CD-NE1). Subsequently, a conformational analysis of (C^2-α-D-Man-)Trp and FTW^{Man}AQW was performed.

An efficient method to study ring flexibility of carbohydrates is high-temperature MD simulation using TINKER/MM3 with a dielectric constant of four. This method gives direct access to free energy profiles or conformational maps based on the Boltzmann equation (Frank et al., 2007). Plotting the z-component of the ring pucker versus the glycosidic torsion ϕ (Figure 3) clearly shows that there is a dependency between the two parameters: if the mannose adopts a $^4C_1$ conformation torsion ϕ_H prefers values around 110° (termed "synC" here, because the Man-C2 atom is approximately in a syn-orientation to the N-atom of the indole moiety) and 270° ("antiC"), whereas for the $^1C_4$ conformation the energy minima are located at about 20° ("synH") and 190° ("antiH"). Consequently, a ring inversion is accompanied by a change of the preferred orientation of the glycosidic torsion. A free energy analysis of the trajectory using the Boltzmann equation reveals that the ring inversion barriers are in the range of 7–8 kcal/mol and that the $^4C_1$ ring conformation is preferred by about 2.0 kcal/mol (Figure S1). Consequently, according to MM3 force field calculations, the bulky 3-methyl-indole substituent can be well accommodated in an axial orientation at the anomeric C-atom. In order to investigate further the effect of substitution at C1 on ring conformation, additional mannosides were also simulated (Figure S1), and it was found that the energy difference between the $^1C_4$ and $^4C_1$ conformation follows as expected the order β-D-Man-OMe > α-D-Man-OMe > α-D-Man-3-methyl-indole > α-D-Man-Trp. However, even for C^2-α-D-mannopyranosyl-L-tryptophan the energy for $^1C_4$ is still higher than for $^4C_1$. Since this appeared to be not in agreement with results from NMR, we investigated the source of the disagreement in more detail. A series of QM energy calculations at the DFT(b3lyp) and LMP2 levels confirmed that in the gas phase the $^4C_1$ conformation is preferred over $^1C_4$ for C^2-α-D-mannopyranosyl-3-methyl-indole (Table S4). However, when the energies were calculated with the PBF solvation model $^1C_4$ becomes preferred over $^4C_1$. This means that, in addition to the ring substitution pattern, the solvent may have a profound effect on the conformational equilibrium. To confirm this finding, we investigated conformational energies also based on MD simulations in explicit solvent. Since MM3 (as implemented in TINKER) is not parameterized for use in explicit solvent we used AMBER (which includes GLYCAM06 parameters for the mannose) and GAFF as implemented in YASARA. Also, with these force fields $^4C_1$ is preferred over $^1C_4$ when the calculations are performed in the gas phase (Figure S2). However, when MD simulations are performed with the AMBER force field in explicit solvent $^1C_4$ is preferred by about 1 kcal/mol (Figure S3), independent of the simulation temperature used. The pucker(z) profiles

	Native	Denatured
Man H1	5.27	5.23
Man H2	4.26	4.45
Man H3	4.13	4.14
Man H4	3.91	3.99
Man H5	ND	3.98
Man H6S	4.55	4.27
Man H6R	3.74	3.76

Table 3. ^{1}H Chemical Shifts (ppm) at 300 K of the *C*-Mannopyranosyl Moiety in Native and Denatured RNase 2

derived at 370, 400, and 500 K are very similar. However, although sampling accumulated 62 μs at 310 K the population of the "skew/boat" conformational states is probably not converged as can be seen from the energy difference of about 1.5 kcal/mol. In general, the ring transition barriers are 1–2 kcal/mol lower than those derived from gas phase simulations. The lowest energy conformational state for C^2-α-D-mannopyranosyl-3-methyl-indole is predicted to be $^{1}C_4$-antiH ($\phi_H \approx 200°$) (Figure S4).

Sampling of accumulated 105 μs at 310 K for (C^2-α-D-Man-)Trp and the glycopeptide FTW^{Man}AQW seems to be sufficient to get converged ring pucker energy profiles. The differences to the profiles obtained at higher temperature are limited to the transition state regions (Figure 4). Finally, the conformational analysis of the glycopeptide FTW^{Man}AQW revealed that the results are very similar to those obtained for (C^2-α-D-Man-)Trp. This means that the peptide does not influence significantly the conformational preferences of the glycosylation site. The lowest energy conformational state for the (C^2-α-D-Man-)Trp moiety is predicted to be $^{1}C_4$-antiH ($\phi_H \approx 200°$) (Figure S5), which is in excellent agreement with NMR results.

Although most of the NMR results would be in agreement with a $^{1}C_4$ ring conformation, the ^{3}J coupling constant for Man H3/H4 is clearly an indication that other conformations need to be present as well. Therefore, in order to estimate the stability of skew/boat conformations, 20 MD simulations were performed where the starting ring conformation was $^{1}S_5$ (Figure 5). In all simulations a transition to a chair conformation occurred in less than 40 ns. Those simulations that were started in $^{1}S_5$-synH typically underwent a transition to $^{1}C_4$; however, for $^{1}S_5$-antiH also a significant number of transitions to $^{4}C_1$ occurred. This behavior can also be seen in the pucker(z) versus ϕ_H plot shown in Figure S5: skew/boat conformations with $\phi_H \approx 200°$ (antiH) seem to have a low energy path to either $^{1}C_4$ or $^{4}C_1$, whereas skew/boat conformations with $\phi_H \approx 10°$ (synH) seem to have only a low energy transition path leading to $^{1}C_4$. In general, the most frequently occurring skew/boat conformation is $^{1}S_3$. As previously outlined, the experimentally determined $^{3}J_{H3/H4}$ of 5.3 Hz cannot be explained by a $^{1}C_4$ conformation alone (predicted $^{3}J_{H3/H4}$ = 2.8 Hz, compare Table S2). The existence of a significant amount of $^{4}C_1$ (predicted $^{3}J_{H3/H4}$ = 8.0 Hz) and/or $^{1}S_3$ (predicted $^{3}J_{H3/H4}$ = 8.9 Hz) conformations in the conformational ensemble could in principle explain an increased average $^{3}J_{H3/H4}$ value. However, based on the energy values only about 10% $^{4}C_1$ and <1% skew/boat conformations would be predicted to be present in the conformational ensemble, which would not be sufficient to raise the average value of $^{3}J_{H3/H4}$ from 2.8 to 5.3 Hz. Additionally, taking into account a significant amount of $^{4}C_1$ or $^{1}S_3$ would also influence the average values of the other ^{3}J constants, and for many of them the agreement with the experimental values would get worse. Therefore, it is difficult to explain the origin of the increased $^{3}J_{H3/H4}$ of 5.3 Hz satisfactorily based on the results from the conformational analysis of the glycopeptide.

Conformational Analysis of RNase 2

Several crystal structures of Eosinophil-Derived Neurotoxin (EDN, alternative name is RNase 2) are available in the Protein Data Bank (PDB). The entry with the highest resolution was used as a basis for modeling (pdb entry 1gqv, resolution 0.98 Å) (Swaminathan et al., 2002). RNase 2 contains four cysteine bridges stabilizing the protein fold as well as five surface-exposed N-glycosylation sites (Asn 17, 59, 65, 84, and 92). The *C*-glycosylation site (Trp7) is located at the start of the first α helix (residues 7–16). The orientation of the Trp7 indole ring is stabilized by hydrophobic interactions with Lys1. However, analysis of the beta factors indicates significant flexibility of the Trp7 side chain as well as the existence of several flexible loops

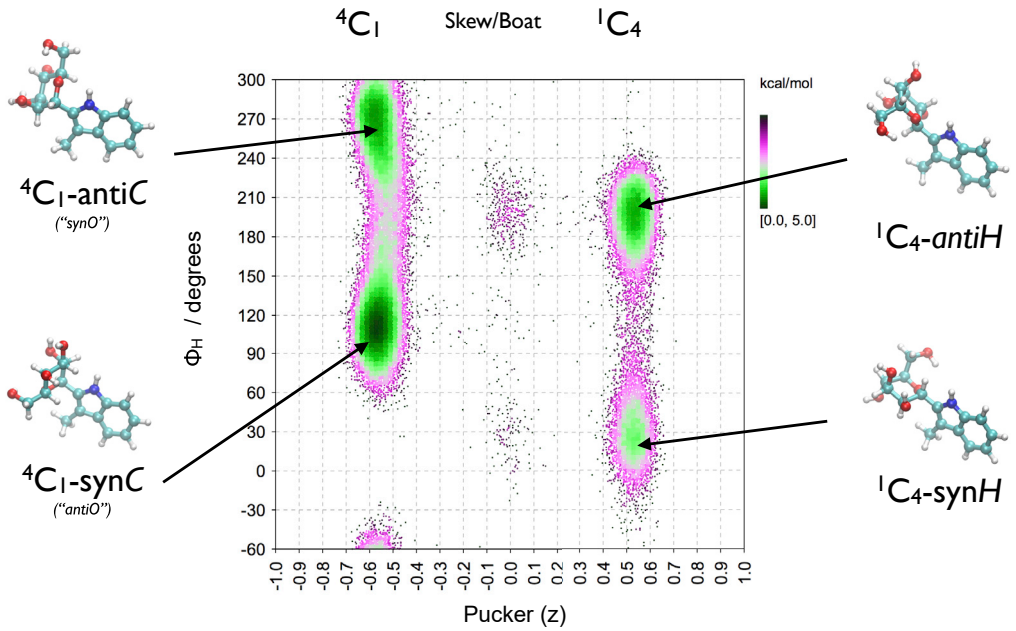

Figure 3. Conformational Preferences of C^2-α-D-mannopyranosyl-3-methyl-indole

Glycosidic torsion ϕ_H as a function of ring pucker coordinate z. Values from 2 μs gas phase MD simulation using TINKER/MM3 (ε = 4) at 400 K. See also Figures S1–S4

(Figure 6). The loop with the highest beta factors (residues 87–96) is involved in binding of the placental ribonuclease inhibitor (Iyer et al., 2005).

C-Mannosylation of Trp7 will most likely have an effect on the dynamics of the Trp7 side chain and the loop consisting of residues 115–123 (termed the "insertion loop" because these residues are not present in RNase 1) and/or the N terminus (residues 1–6) (Figure 6). Since beta factors give only an indication of protein dynamics in the crystal environment, the dynamics of RNase2 in solution was investigated by MD simulation in explicit solvent on the microsecond timescale. In total 23 μs were sampled, and in general the observed dynamics agrees well with the beta factor values of the crystal structure; however, in some of the MD simulations performed significant, but mostly reversible, conformational changes occur in the insertion loop (Figure S6). As an example, the "RMSD per residue" plot of one of the MD simulations (3.7 μs) is shown in Figure 7. It can be observed that the first conformational change, occurring after about 1 μs , was reversible (with a lifetime about 200 ns). However, when the conformational change occurred the second time (at about 1.8 μs) it was not reversible for at least 2 μs. Finally, significant conformational changes occurred also in the N terminus, which made it unlikely that the RNase would recover the crystallographic conformation within a feasible simulation time, so this simulation was not continued. That major conformational changes can occur in the insertion loop was additionally confirmed with MD

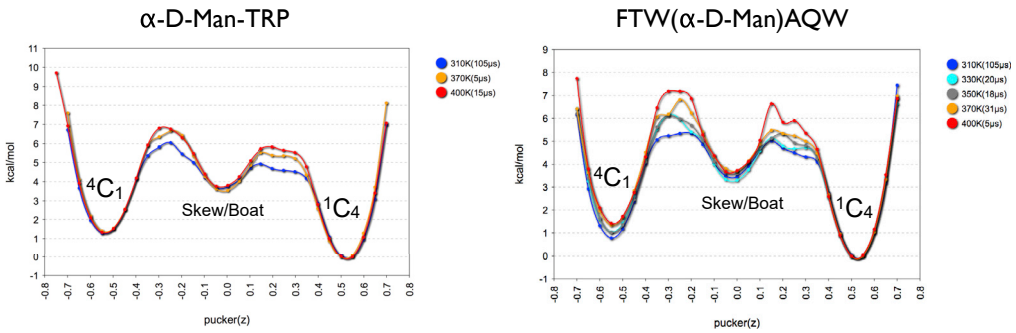

Figure 4. Conformational Ring Transition Energy Profiles of (C^2-α-D-Man-)Trp

Calculated in explicit solvent at various temperatures (AMBER, NPT/NVT ensemble). See also Figure S5

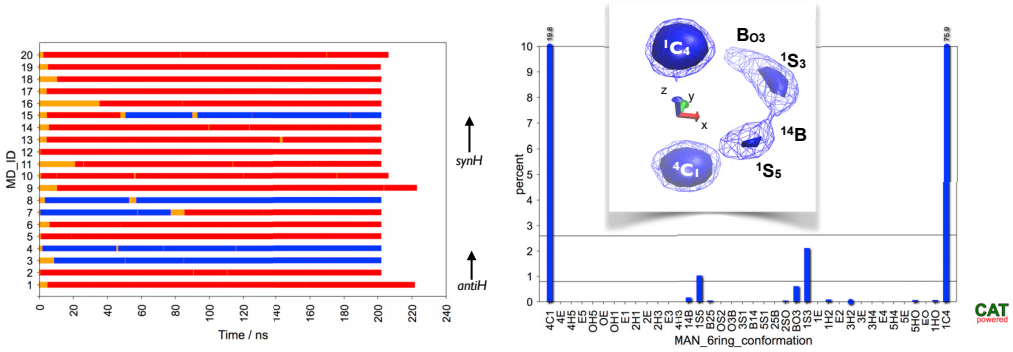

Figure 5. Stability Check of "Skew/Boat" Conformations for Glycopeptide FTW^{Man}AQW

Based on MD simulations in explicit solvent at 310 K (20 × 0.2 μs, AMBER, NPT ensemble). Left: Simplified representation of ring conformation trajectories (orange: skew/boat, red: $^{1}C_{4}$, blue: $^{4}C_{1}$). Right: population of ring conformational states. Insert: Iso-contour plot indicating the location of the minima in ring pucker space.

simulations using other force fields such as OPLS-AA and CHARMM (data not shown); by consequence this result is not an artifact of the Amber force field used.

In the next step an α-mannose residue was linked to Trp7 and it was examined whether the presence of the α-mannose would stabilize the insertion loop and also the N-terminal residues. In general, it was found that the α-mannose moiety could be accommodated without steric clashes and in all four conformational states ($^{1}C_{4}$-synH, $^{1}C_{4}$-antiH, $^{4}C_{1}$-synC, $^{4}C_{1}$-antiC) in the cleft formed between Trp7 and Asp112–Arg118 (Figure 8). Therefore, multiple MD simulations were started for each of these conformational states in order to investigate their stability and dynamics. MD simulations revealed that a significant stabilization of the protein occurred only when the α-mannose was linked in a $^{1}C_{4}$-synH conformation. The insertion loop maintained its conformation significantly better than in the simulations without α-mannose (apo) or with α-mannose in a $^{1}C_{4}$-antiH conformation (Figure 9).

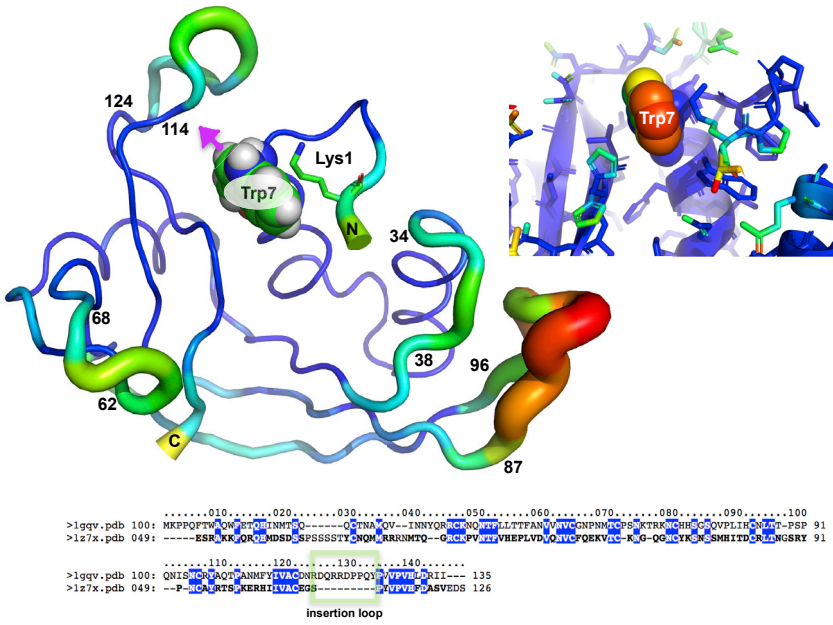

Figure 6. Crystal Structure of Eosinophil-Derived Neurotoxin (EDN, RNase 2)

Based on pdb code 1gqv (Swaminathan et al., 2002). Top left: Protein flexibility (beta factor) is indicated by the thickness and color of the backbone representation (PyMol "putty" representation). Top right: Crystallographic beta factors mapped to the atoms as a color code. Red color indicates a high beta factor value. TRP7 is shown as CPK. The arrow denotes the attachment point of α-mannose (C-glycosylation site). Bottom: Structure-based sequence alignment (Jung and Lee, 2000) of RNase 1 (sequence taken from PDB entry 1z7x) and RNase 2 (sequence taken from PDB entry 1gqv).

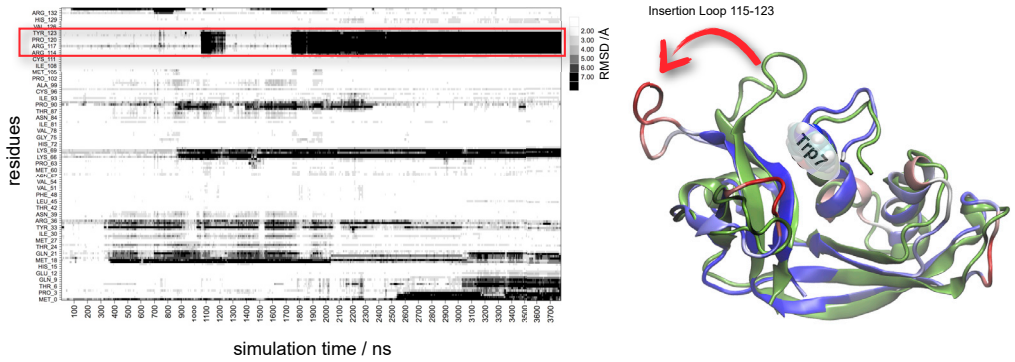

Figure 7. Dynamics of RNase 2 as Shown from MD Simulations on the Microsecond Timescale

Left: "RMSD per residue" trajectory plot. Major conformational change (shown by a change to black coloring) of the insertion loop (residue 115–123, indicated by the boxed area) occurs at 1.1 (reversible) and 1.8 μs (irreversible). Right: RNase 2 shown as a cartoon representation. The starting structure of the MD is shown in green. The last snapshot of the trajectory is superimposed and colored by RMSD (blue-white-red, interval 0–7 Å). The change of the insertion loop orientation and the location of Trp7 are indicated. See also Figure S6.

When the simulations are performed with mannose in a $^{1}C_{4}$-antiH conformation the mannose residue and the insertion loop are significantly more dynamic. During the 12 μs sampled several reversible transitions to skew/boat conformations occurred. Such transitions did not occur during the 10 μs sampled with mannose in a $^{1}C_{4}$-synH conformation (Figure S7). In general, it was found that $^{4}C_{1}$ ring conformations of C-linked mannose are significantly less stable in RNase 2 than in the glycopeptide FTW^{Man}AQW. An extensive analysis involving more than hundred MD simulations of *C*-mannosylated RNase 2 revealed that $^{4}C_{1}$-synC is more stable than $^{4}C_{1}$-antiC, and typically irreversible transitions to $^{1}C_{4}$ occurred always in less than 100 ns (Figures S8 and S9). In contrast, for the glycopeptide the chair form $^{4}C_{1}$ was found to be stable sometimes longer than 1 μs. An additional extensive investigation consisting of 60 MD simulations on the stability of skew/boat forms revealed that $^{1}S_{3}$ is the most populated skew/boat form and that the lifetime of skew/boat forms is four times longer when ϕ_H is in syn orientation (Figure S10). In general, the MD data reveal that in the context of the RNase 2, the lifetime of $^{4}C_{1}$ is significantly shorter than in the free glycopeptide and the skew/boat conformational state does have a similar lifetime.

It should be noted that during the accumulated 22 μs sampled for αMan($^{1}C_{4}$)-RNase 2 no transition between antiH and synH occurred. Since also the $^{4}C_{1}/^{1}C_{4}$ transitions were irreversible on the microsecond

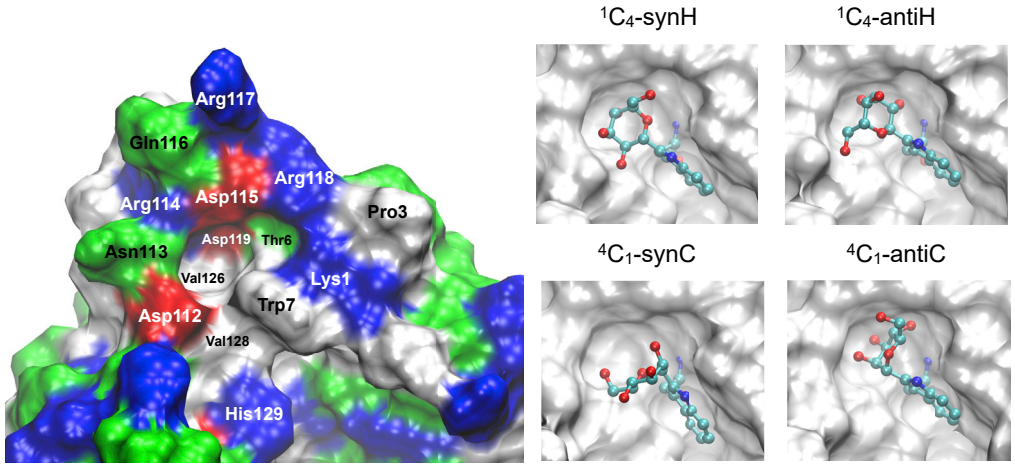

Figure 8. Surface Representation Showing the Cleft Formed between Trp7 and the "Insertion Loop" (Asp112–Arg118)

Left: Amino acids are colored by type: negatively charged (red), positively charged (blue), polar (green), lipophilic (white). Right: α-Mannose attached to Trp7 in various conformational states (see text for details). Atoms are colored by element: carbon (cyan), oxygen (red), nitrogen (blue).

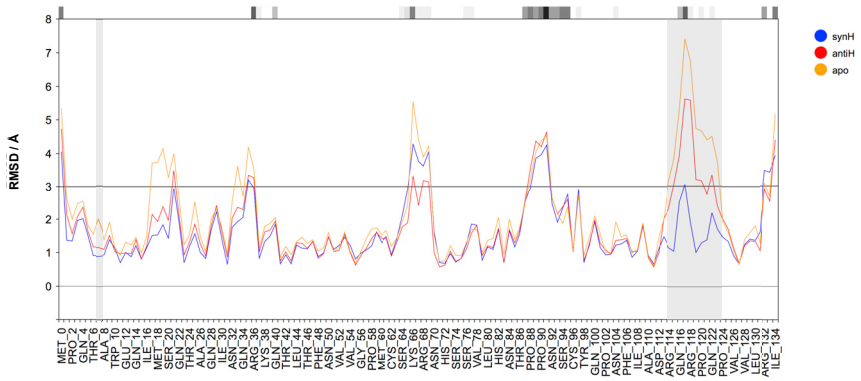

Figure 9. Differences in Average RMSD (C-Alpha Atoms) between $^{1}C_{4}$-Mannosylated RNase and "Apo" RNase 2
A slight reduction in RMSD occurs for Trp7 (highlighted with gray background), but a significant decrease in RMSD is evident for the insertion loop (residues 114–124, highlighted with gray background) when α-mannose is linked in a $^{1}C_{4}$-synH conformation. The X-ray beta factors of the residues are indicated as a grayscale annotation bar above the plot (darker gray means higher value). See also Figure S7.

timescale this means that it is currently unfeasible to directly determine the free energy landscape of the various conformational states of *C*-mannosylated RNase 2 by population statistics using the Boltzmann equation. However, the extensive MD data clearly show that $^{1}C_{4}$-synH is the most stable conformational state of *C*-mannosylated RNase 2: within the accumulated 10 μs sampled for αMan($^{1}C_{4}$-synH)-RNase2 the α-mannose remained in this state and formed several very stable hydrogen bonds with the protein (Figure 10, Tables S5, and S6). Of particular interest are the hydrogen bonds between Man O6 and Asp115/Arg118, which directly stabilize the conformation of the insertion loop. The CH-π interactions between the indole moiety of Trp7 and the aliphatic side chain CH atoms of Lys1 are likely to be critical stabilization factors for the conformation of the N-terminal residue. Since the H-bond between the ring oxygen and Trp7 backbone nitrogen stabilizes directly the side chain conformation of Trp7, the existence of the C-linked α-mannose has most likely also an indirect stabilization effect on the N terminus (residues 1–6) of RNase 2.

Finally, the conformational state $^{1}C_{4}$-synH in native RNase is also in excellent agreement with NMR results (Tables 1 and S7).

DISCUSSION

The function of *C*-mannosylation has not been fully elucidated, but studies conducted so far indicate that it plays an important role in protein folding, targeting of substrate proteins, or regulating cellular signaling (Ihara et al., 2015). Hartmann and Hofsteenge (2000) supposed that the 14 mannose residues linked to properdin could be exposed at the surface of the protein thanks to their hydrophilic character and therefore mediate properdin interaction with the multivalent mannose-binding lectin present in serum. Differently from properdin, in RNase 2 the accessibility of the mannose residue is quite poor. In RNase 2 and EDN, the presence of *C*-mannose seems not to be related directly to any specific biological function. Comparison of enzymatic activity of recombinant RNase from *Escherichia coli* with the *C*-mannosylated RNase 2 could not elucidate significant differences (Furmanek and Hofsteenge, 2000). Similarly, *C*-mannose does not seem to be essential for the neurotoxic activity of EDN, since the related RNase eosinophil cationic protein, which contains an arginine at position 7 instead of (C^{2}-α-D-Man-)Trp, is equally toxic (Snyder and Gleich, 1997).

Biophysical and biochemical studies show that glycosylation facilitates the folding and increases the stability of some proteins (Kassenbrock et al., 1988; Imperiali and Rickert, 1995), and *C*-mannosylation of thrombospondin type 1 repeats imparts higher resistance to thermal and reductive denaturation processes (Shcherbakova et al., 2019). Therefore, it could be hypothesized that C-linked mannose may similarly exert a structural function in RNase 2.

(C^{2}-α-D-Man-)Trp is located in the N-terminal α-helix of RNase 2. The three dimensional structure of rEDN has been compared with that of bovine pancreatic RNase A, which lacks the (C^{2}-α-D-Man-)Trp moiety (Mosimann et al., 1996). Although the α helices and the β strands are almost identical in the two proteins, the N-terminal loop and the large insertion loop are absent in RNase A. NMR and molecular simulation studies demonstrated

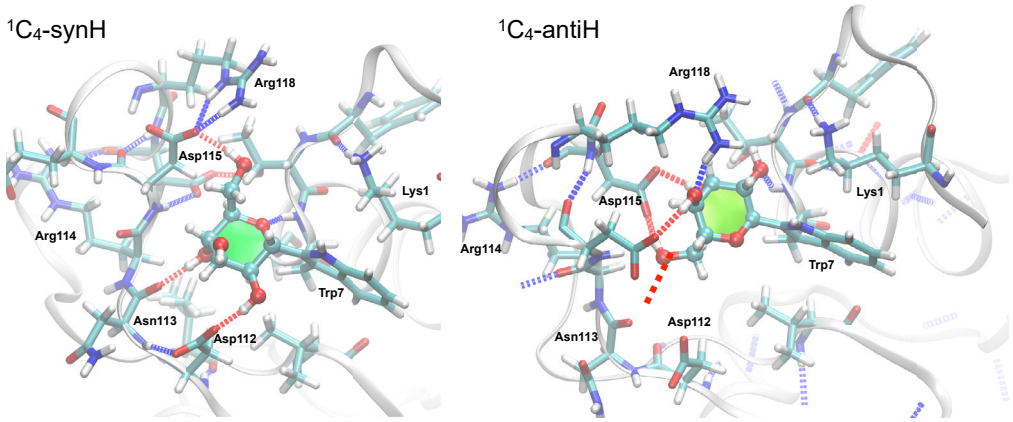

Figure 10. C-Linked α-mannose ($^1C_4$) Forms an Extensive Network of Hydrogen Bonds with RNase 2
See also Tables S5 and S6.

that the presence of *C*-mannose stabilizes the conformation of the large insertion loop and also the N-terminal loop. In principle, the *C*-mannose can be accommodated in the cleft formed between Trp 7 and Asp 112–118 without steric clashes and links the N-terminal residues with residues 112–115 through a specific network of hydrogen bonds in a "lock-and-key"-like manner. In this study we investigated the conformational preferences of *C*-mannosylated tryptophan and its impact on the stability of RNase 2 by NMR and extensive MD simulation. In NOESY spectra, an intense NOE between mannose H1 and H6 clearly indicates that the hydroxymethyl group is not in the usual equatorial orientation, which is typical of the $^4C_1$ conformation, but in the axial orientation typical of the $^1C_4$ chair. Surprisingly, the correct energy ranking of the chair forms could only be obtained when solvent was taken into account in the calculations. Consequently, the bulky axial substituent at the anomeric C-atom seems to be insufficient to change the conformational equilibrium to favor $^1C_4$. In general, the conformational analysis based on MD simulations in explicit solvent has been computationally very challenging (many months of calculation time) because hundreds of microseconds had to be sampled to obtain sufficiently converged results. This has become feasible only recently owing to a significant advance in computer hardware (fast GPUs), MD software (e.g., YASARA) and high-performance analysis software (Conformational Analysis Tools) that allow one to calculate and analyze hundreds of GBytes of trajectory data and assemble the results of hundreds of MD simulations efficiently. It is encouraging that such high-level MD simulations (physiological conditions, sampling on the microsecond timescale) can give valuable insights into the dynamics of glycoproteins that seem to be sufficiently reliable and that can currently not be obtained with any other experimental method.

To achieve an optimal conformational fit, the mannose has to adopt a $^1C_4$-synH conformational state. NMR and MD simulations show that $^1C_4$-antiH is preferred in unfolded RNase 2 (and in glycopeptides), which raises the intriguing question how such a conformational change may occur. Microsecond MD simulations show that the insertion loop and the mannose orientation are more flexible for $^1C_4$-antiH; therefore, the nascently folded RNase 2 may undergo a self-optimization process where the $^1C_4$-synH and the insertion loop get locked after the antiH/synH conformational transition has occurred.

It may be concluded that the main role of the mannose is to stabilize the N-terminal loop of the protein by moderating the interaction with the large insertion loop, whose presence has been hypothesized to contribute to the antiviral properties of EDN (Domachowske et al., 1998). This hypothesis finds support in the behavior of other glycoproteins, such as the proteinase inhibitor PMP-C, where the fucose residue linked to Thr9 causes a decrease in the number of dynamic fluctuations of the molecule (Mer et al., 1996).

Limitations of the Study

This study does not provide experimental evidence that *C*-mannosylation enhances the structural stability of RNase 2. Although the MD simulations presented here are very extensive, it is currently technically unfeasible to sample the conformational equilibrium of the different chair conformations of mannose when attached to RNase 2.

Resource Availability

Lead Contact

Johannes F.G. Vliegenthart, j.f.g.vliegenthart@uu.nl.

Materials Availability

This study did not generate new unique reagents.

Data and Code Availability

The datasets supporting the current study have not been deposited in a public repository because they are too large (terabytes) but are available from the corresponding author on request.

The software Conformational Analysis Tools (CAT) used for analysis of the MD trajectories is developed by Martin Frank and is freely available at http://www.md-simulations.de/CAT/

METHODS

All methods can be found in the accompanying Transparent Methods supplemental file.

SUPPLEMENTAL INFORMATION

Supplemental Information can be found online at https://doi.org/10.1016/j.isci.2020.101371.

ACKNOWLEDGMENTS

This work has been supported financially by the CARENET 2 European network (HPRN-CT-2000-000001). We would like to thank Dr. S. Meunier for helping us in processing the NMR data and Dr. S. Mosimann and M. James for the communication of the three-dimensional structure of rEDN. The authors are grateful to Dr. J. Hofsteenge for proving a sample of RNase 2 and glycopeptide fragments.

AUTHOR CONTRIBUTIONS

M.F. performed the molecular dynamics simulations and computational analysis. D.B. and B.R.L. conducted the NMR studies. J.F.G.V. conceived the project. All authors contributed to manuscript writing and revision.

DECLARATION OF INTEREST

The authors declare no competing interests.

Received: March 20, 2020
Revised: June 22, 2020
Accepted: July 13, 2020
Published: August 21, 2020

REFERENCES

Agirre, J., Davies, G.J., Wilson, K.S., and Cowtan, K.D. (2017). Carbohydrate structure: the rocky road to automation. Curr. Opin. Struct. Biol. *44*, 39–47.

Aleshin, A.E., Schraufstatter, I.U., Stec, B., Bankston, L.A., Liddington, R.C., and DiScipio, R.G. (2012). Structure of complement C6 suggests a mechanism for initiation and unidirectional, sequential assembly of membrane attack complex (MAC). J. Biol. Chem. *287*, 10210–10222.

De Beer, T., Vliegenthart, J.F., Löffler, A., and Hofsteenge, J. (1995). The hexopyranosyl residue that is C-glycosidically linked to the side chain of tryptophan-7 in human RNase Us is alpha-mannopyranose. Biochemistry *34*, 11785–11789.

van den Bos, R.M., Pearce, N.M., Granneman, J., Brondijk, T.H.C., and Gros, P. (2019). Insights into enhanced complement activation by structures of properdin and its complex with the C-terminal domain of C3b. Front. Immunol. *10*, 785.

Buettner, F.F., Ashikov, A., Tiemann, B., Lehle, L., and Bakker, H. (2013). C. elegans DPY-19 is a C-mannosyltransferase glycosylating thrombospondin repeats. Mol. Cell *50*, 295–302.

Domachowske, J.B., Dyer, K.D., Bonville, C.A., and Rosenberg, H.F. (1998). Recombinant human eosinophil-derived neurotoxin/RNase 2 functions as an effective antiviral agent against respiratory syncytial virus. J. Infect. Dis. *177*, 1458–1464.

Doucey, M.A., Hess, D., Cacan, R., and Hofsteenge, J. (1998). Protein C-mannosylation is enzyme-catalysed and uses dolichyl-phosphate-mannose as a precursor. Mol. Biol. Cell *9*, 291–300.

Doucey, M.A., Hess, D., Blommers, M.J., and Hofsteenge, J. (1999). Recombinant human interleukin-12 is the second example of a C-mannosylated protein. Glycobiology *9*, 435–441.

Falzarano, D., Krokhin, O., Van Domselaar, G., Wolf, K., Seebach, J., Schnittler, H.J., and Feldmann, H. (2007). Ebola sGP—the first viral glycoprotein shown to be C-mannosylated. Virology *368*, 83–90.

Frank, M., Lutteke, T., and von der Lieth, C.W. (2007). GlycoMapsDB: a database of the accessible conformational space of glycosidic

linkages. Nucleic Acids Res. *35* (Database issue), 287–290.

Furmanek, A., and Hofsteenge, J. (2000). Protein C-mannosylation: facts and questions. Acta Biochimica Pol *47*, 781–789.

Furmanek, A., Hess, D., Rogniaux, H., and Hofsteenge, J. (2003). The WSAWS motif is C-hexosylated in a soluble form of the erythropoietin receptor. Biochemistry *42*, 8452–8458.

Gonzalez de Peredo, A., Klein, D., Macek, B., Hess, D., Peter-Katalinic, J., and Hofsteenge, J. (2002). C-mannosylation and o-fucosylation of thrombospondin type 1 repeats. Mol. Cell Proteomics *1*, 11–18.

Goto, Y., Niwa, Y., Suzuki, T., Dohmae, N., Umezawa, K., and Simizu, S. (2014). C-mannosylation of human hyaluronidase 1: possible roles for secretion and enzymatic activity. Int. J. Oncol. *45*, 344–350.

Hadders, M.A., Bubeck, D., Roversi, P., Hakobyan, S., Forneris, F., Morgan, B.P., Pangburn, M.K., Llorca, O., Lea, S.M., and Gros, P. (2012). Assembly and regulation of the membrane attack complex based on structures of C5b6 and sC5b9. Cell Rep. *1*, 200–207.

Hamann, K.J., Barker, R.L., Loegering, D.A., Pease, L.R., and Gleich, G.J. (1989). Sequence of human eosinophil-derived neurotoxin cDNA: identity of deduced amino acid sequence with human nonsecretory ribonucleases. Gene *83*, 161–167.

Hamming, O.J., Kang, L., Svensson, A., Karlsen, J.L., Rahbek-Nielsen, H., Paludan, S.R., Hjorth, S.A., Bondensgaard, K., and Hartmann, R. (2012). Crystal structure of interleukin-21 receptor (IL-21R) bound to IL-21 reveals that sugar chain interacting with WS XWS motif is integral part of IL-21R. J. Biol. Chem. *287*, 9454–9460, Available at: http://www.jbc.org/lookup/doi/10.1074/jbc.M111.311084.

Hartmann, S., and Hofsteenge, J. (2000). Properdin, the positive regulator of complement, is highly C-mannosylated. J. Biochem. *275*, 28569–28574.

Hofsteenge, J., Müller, D.R., de Beer, T., Löffler, A., Richter, W.J., and Vliegenthart, J.F. (1994). New type of linkage between a carbohydrate and a protein: C-glycosylation of a specific tryptophan residue in human RNase Us. Biochemistry *33*, 13524–13530.

Hinou, H., Abe, Y., Hayakawa, S., Naruchi, K., Fujitani, N., and Nishimura, S.-I. (2016). Solid-phase synthesis of C-mannosylated glycopeptide on WSXWS motif of human erythropoietin receptor. Tetrahedron Lett. *57*, 791–795.

Hofsteenge, J., Blommers, M., Hess, D., Furmanek, A., and Miroshnichenko, O. (1999). The four terminal components of the complement system are C-mannosylated on multiple tryptophan residues. J. Biochem. *274*, 32786–32794.

Hofsteenge, J., Huwiler, K.G., Macek, B., Hess, D., Lawler, J., Mosher, D.F., and Peter-Katalinic, J. (2001). C-mannosylation and O-fucosylation of the thrombospondin type 1 module. J. Biochem. *276*, 6485–6498.

Ihara, Y., Manabe, S., Kanda, M., Kawano, H., Nakayama, T., Sekine, I., Kondo, T., and Ito, Y. (2005). Increased expression of protein C-mannosylation in the aortic vessels of diabetic Zucker rats. Glycobiology *15*, 383–392.

Ihara, Y., Inai, Y., Ikezaki, M., Matsui, I.-S.L., Manabe, S., and Ito, Y. (2015). C-Mannosylation: Modification on Tryptophan in Cellular Proteins. In Biology and Medicine, T. Endo, H.P. Seeberger, W.G. Hart, C.H. Wong, N. Taniguchi, and Glycoscience., eds. (Springer), pp. 1091–1099.

Ihara, Y., Manabe, S., Ikezaki, M., Inai, Y., Matsui, I.S., Ohta, Y., Muroi, E., and Ito, Y. (2010). C-Mannosylated peptides derived from the thrombospondin type 1 repeat interact with Hsc70 to modulate its signaling in RAW264.7 cells. Glycobiology *20*, 1298–1310.

Imperiali, B., and Rickert, K.W. (1995). Conformational implications of asparagine-linked glycosylation. Proc. Natl. Acad. Sci. U S A *92*, 97–101.

Iyer, S., Holloway, D.E., Kumar, K., Shapiro, R., and Acharya, K.R. (2005). Molecular recognition of human eosinophil-derived neurotoxin (RNase 2) by placental ribonuclease inhibitor. J. Mol. Biol. *347*, 637–655.

Julenius, K. (2007). NetCGlyc 1.0: prediction of mammalian C-mannosylation sites. Glycobiology *17*, 868–876.

Jung, J., and Lee, B. (2000). Protein structure alignment using environmental profiles. Protein Eng. *13*, 535–543.

Kassenbrock, C.K., Garcia, P.D., Walter, P., and Kelly, R.B. (1988). Heavy-chain binding protein recognizes aberrant polypeptides translocated in vitro. Nature *333*, 90–93.

Klein, C., Waldhauer, I., Nicolini, V.G., Freimoser-Grundschober, A., Nayak, T., Vugts, D.J., Dunn, C., Bolijn, M., Benz, J., Stihle, M., et al. (2017). Cergutuzumab amunaleukin (CEA-IL2v), a CEA-targeted IL-2 variant-based immunocytokine for combination cancer immunotherapy: overcoming limitations of aldesleukin and conventional IL-2-based immunocytokines. Oncoimmunology *6*, e1277306.

Krieg, J., Gläsner, W., Vicentini, A., Doucey, M.A., Löffler, A., Hess, D., and Hofsteenge, J. (1997). C-Mannosylation of human RNase 2 is an intracellular process performed by a variety of cultured cells. J. Biol. Chem. *272*, 26687–26692.

Krieg, J., Hartmann, S., Vicentini, A., Gläsner, W., Hess, D., and Hofsteenge, J. (1998). Recognition signal for C-mannosylation of Trp-7 in RNase 2 consists of sequence Trp-x-x-Trp. Mol. Biol. Cell *9*, 301–309.

Li, Y., Cao, C., Jia, W., Yu, L., Mo, M., Wang, Q., Huang, Y., Lim, J.M., Ishihara, M., Wells, L., et al. (2009). Structure of the F-spondin domain of mindin, an integrin ligand and pattern recognition molecule. EMBO J. *28*, 286–297.

Löffler, A., Doucey, M.A., Jansson, A.M., Müller, D.R., de Beer, T., Hess, D., Meldal, M., Richter, W.J., Vliegenthart, J.F., and Hofsteenge, J. (1996). Spectroscopic and protein chemical analyses demonstrate the presence of C-mannosylated tryptophan in intact human RNase 2 and its isoforms. Biochemistry *35*, 12005–12014.

Lovelace, L.L., Cooper, C.L., Sodetz, J.M., and Lebioda, L. (2011). Structure of human C8 protein provides mechanistic insight into membrane pore formation by complement. J. Biol. Chem. *286*, 17585–17592.

Manabe, S., and Ito, Y. (1999). Total synthesis of novel subclass of glyco-amino acid structure motif: C2-α- l- C-mannosylpyranosyl-l-tryptophan. J. Am. Chem. Soc. *121*, 9754–9755.

Mer, G., Hietter, H., and Lefevre, J.F. (1996). Stabilization of proteins by glycosylation examined by NMR analysis of a fucosylated proteinase inhibitor. Nat. Struct. Biol. *3*, 45–53.

Mosimann, S.C., Newton, D.L., Youle, R.J., and James, M.N. (1996). X-ray crystallographic structure of recombinant eosinophil-derived neurotoxin at 1.83 A resolution. J. Mol. Biol. *260*, 540–552.

Munte, C.E., Gäde, G., Domogalla, B., Kremer, W., Kellner, R., and Kalbitzer, H.R. (2008). C-mannosylation in the hypertrehalosaemic hormone from the stick insect Carausius morosus. FEBS J. *275*, 1163–1173.

Niwa, Y., Suzuki, T., Dohmae, N., and Simizu, S. (2016). Identification of DPY19L3 as the C-mannosyltransferase of R-spondin1 in human cells. Mol. Biol. Cell *27*, 744–756.

Okamoto, S., Murano, T., Suzuki, T., Uematsu, S., Niwa, Y., Sasazawa, Y., Dohmae, N., Bujo, H., and Simizu, S. (2017). Regulation of secretion and enzymatic activity of lipoprotein lipase by C-mannosylation. Biochemical and Biophysical Research Communications *486*, 558–563.

Otani, K., Niwa, Y., Suzuki, T., Sato, N., Sasazawa, Y., Dohmae, N., and Simizu, S. (2018). Regulation of granulocyte colony-stimulating factor receptor-mediated granulocytic differentiation by C-mannosylation. Biochem. Biophys. Res. Commun. *498*, 466–472.

Pedersen, D.V., Gadeberg, T.A.F., Thomas, C., Wang, Y., Joram, N., Jensen, R.K., Mazarakis, S.M.M., Revel, M., El Sissy, C., Petersen, S.V., et al. (2019). Structural basis for properdin oligomerization and convertase stimulation in the human complement system. Front. Immunol. *10*, 2007.

Perez-Vilar, J., Randell, S.H., and Boucher, R.C. (2004). C-Mannosylation of MUC5AC and MUC5B Cys subdomains. Glycobiology *14*, 325–337.

Pronker, M.F., Lemstra, S., Snijder, J., Heck, A.J., Thies-Weesie, D.M., Pasterkamp, R.J., and Janssen, B.J. (2016). Structural basis of myelin-associated glycoprotein adhesion and signalling. Nat. Commun. *7*, 1–13.

Sasazawa, Y., Sato, N., Suzuki, T., Dohmae, N., and Simizu, S. (2015). C-Mannosylation of thrombopoietin receptor (c-Mpl) regulates thrombopoietin-dependent JAK-STAT signaling. Biochem. Biophys. Res. Commun. *468*, 262–268.

Shcherbakova, A., Preller, M., Taft, M.H., Pujols, J., Ventura, S., Tiemann, B., Buettner, F.F.R., and Bakker, H. (2019). C-mannosylation supports folding and enhances stability of thrombospondin repeats. Elife *8*, 10210.

Shcherbakova, A., Tiemann, B., Buettner, F.F., and Bakker, H. (2017). Distinct C-mannosylation of netrin receptor thrombospondin type 1 repeats by mammalian DPY19L1 and DPY19L3. Proc. Natl. Acad. Sci. U S A *114*, 2574–2579.

Snyder, M.R., and Gleich, G.J. (1997). Ribonucleases, structures and functions. In Ribonucleases, Structures and Functions, G. D'Alessio and J.F. Riordan, eds. (Academic Press, Inc.), pp. 425–444.

Spiro, R.G. (2002). Protein glycosylation: nature, distribution, enzymatic formation, and disease implications of glycopeptide bonds. Glycobiology *12*, 43R–56R.

Swaminathan, G.J., Holloway, D.E., Veluraja, K., and Acharya, K.R. (2002). Atomic resolution (0.98 Å) structure of eosinophil-derived neurotoxin. Biochemistry *41*, 3341–3352.

Tan, K., Duquette, M., Liu, J.H., Dong, Y., Zhang, R., Joachimiak, A., Lawler, J., and Wang, J.H. (2002). Crystal structure of the TSP-1 type 1 repeats: a novel layered fold and its biological implication. J. Cell Biol. *159*, 373–382.

Vliegenthart, J.F., and Casset, F. (1998). Novel forms of protein glycosylation. Curr. Opin. Struct. Biol. *8*, 565–571.

Wang, L.W., Leonhard-Melief, C., Haltiwanger, R.S., and Apte, S.S. (2009). Post-translational modification of thrombospondin type-1 repeats in ADAMTS-like 1/punctin-1 by C-mannosylation of tryptophan. J. Biol. Chem. *284*, 30004–30015.

Yoon, C., Johnston, S.C., Tang, J., Stahl, M., Tobin, J.F., and Somers, W.S. (2000). Charged residues dominate a unique interlocking topography in the heterodimeric cytokine interleukin-12. EMBO J. *19*, 3530–3541.

iScience, Volume *23*

Supplemental Information

C-Mannosylation Enhances the Structural Stability of Human RNase 2

Martin Frank, Daniela Beccati, Bas R. Leeflang, and Johannes F.G. Vliegenthart

Supplemental Figures

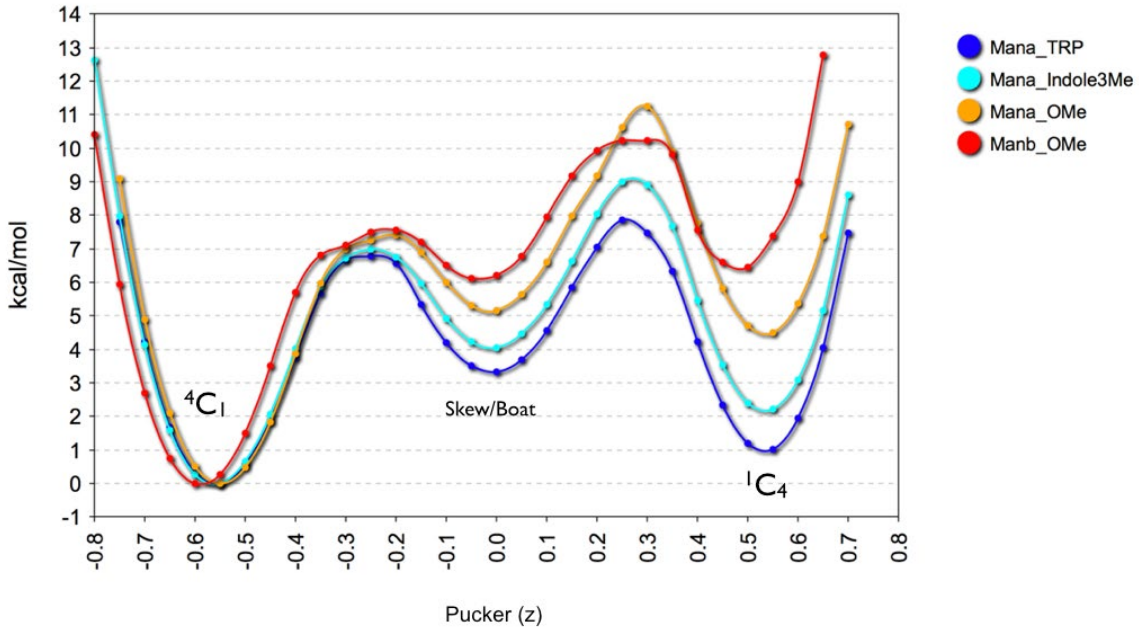

Figure S1: Ring conformational energies as a function of ring pucker coordinate z for various D-mannopyranosyl compounds. Related to Figure 3.
Calculated from gas phase MD simulations using TINKER/MM3 (ε = 4) at 500 K. Energy difference between the $^1C_4$ and $^4C_1$ conformation follows as expected the order β-D-Man-OMe > α-D-Man-OMe > α-D-Man-3-methyl-indole > α-D-Man-Trp.

AMBER14/YASARA 310K

group	counts	E_sys_MD	E_sys_MIN
4C1_synC	200	5.0 ± 0.9	1.5 ± 0.7
4C1_synO	200	0.0 ± 1.0	0.0 ± 0.1
1C4_antiH	285	6.0 ± 1.6	1.8 ± 0.5
1C4_synH	115	8.7 ± 1.2	4.2 ± 0.2

GAFF/YASARA 310K

group	counts	E_sys_MD	E_sys_MIN
4C1_synC	198	2.1 ± 1.3	0.4 ± 0.6
4C1_synO	202	0.0 ± 0.7	0.0 ± 0.2
1C4_antiH	200	3.3 ± 1.5	2.8 ± 0.3
1C4_synH	200	10.3 ± 1.2	7.5 ± 0.1

minimized

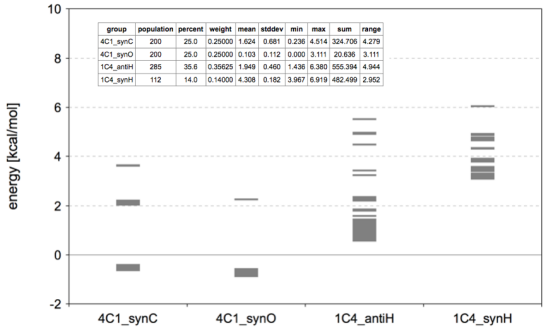

minimized

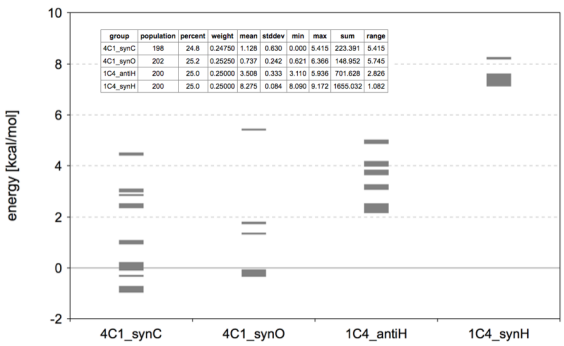

Figure S2: Conformational state energies of *C*^{2}-α-D-mannopyranosyl-3-methyl-indole calculated in the gas phase with AMBER(Glycam-06) and GAFF. Related to Figure 3.
Values are derived by calculating the relative force field energies of the MD snapshots directly and after energy minimization. The values are grouped into the four conformational states shown in Figure 3. $^4C_1$(synO) has consistently the lowest average force field energy. However, for GAFF some of the minimized frames belonging to the $^4C_1$(synC) state have lower energy than the energy minimum of the $^4C_1$(synO) states. It is obvious that there are significant differences in the minimized energies within a conformational state, which is most likely caused by different orientations of the OH-groups of the mannose. This highlights the difficulties involved in deriving reliable relative force field energies. Despite this it can be concluded that in the gas phase $^4C_1$ is preferred over $^1C_4$ for both force fields used.

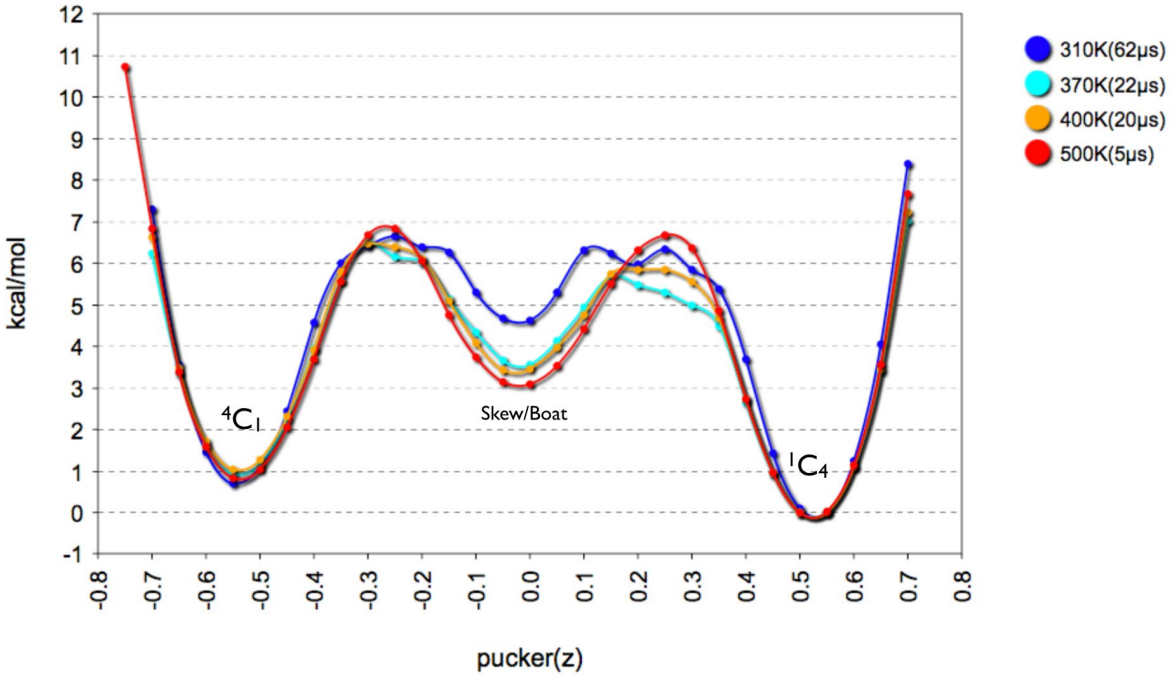

Figure S3: Conformational ring transition profiles of *C*^{2}-α-D-mannopyranosyl-3-methyl-indole. Related to Figure 3.
Calculated in explicit solvent at various temperatures (AMBER, NVT ensemble).

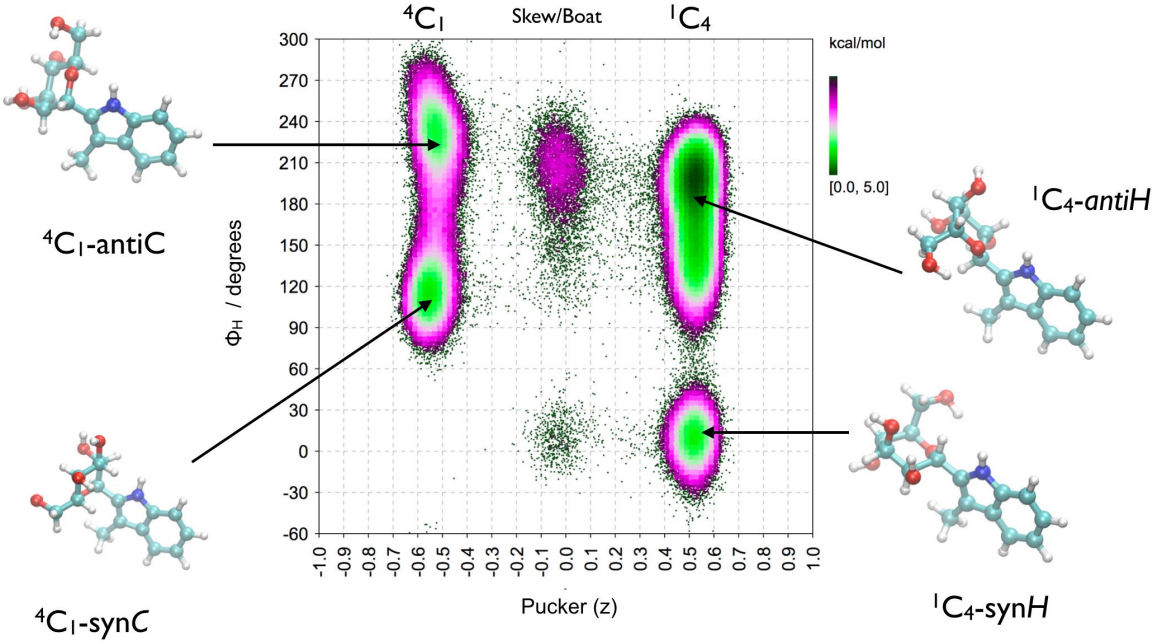

Figure S4: Conformational preferences of *C*^{2}-α-D-mannopyranosyl-3-methyl-indole as a function of ring puckering coordinate z and glycosidic torsion φ_H. Related to Figure 3.
Values from 63 µs MD simulation in explicit solvent at 310 K (AMBER, NPT ensemble).

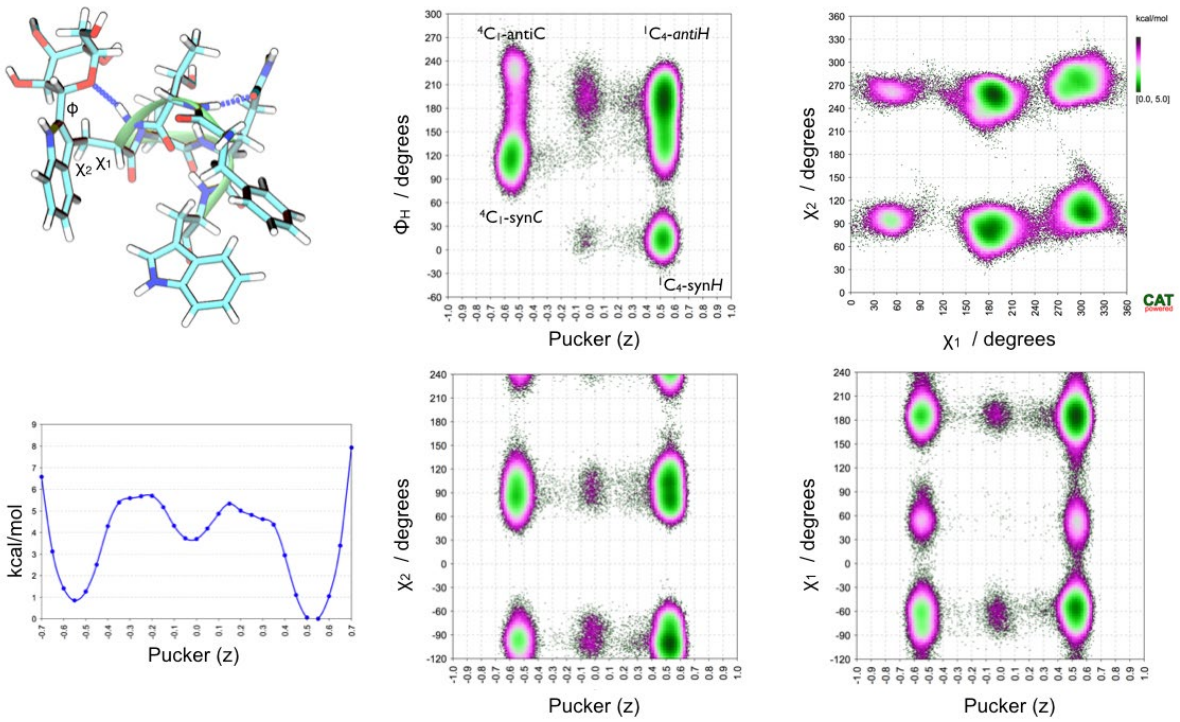

Figure S5: Conformational analysis of FTW^{Man}AQW. Related to Figure 4.
Calculated from MD simulation in explicit solvent at 310 K (105 µs, AMBER, NPT ensemble). χ_1 and χ_2 do not seem to be significantly incluenced by the ring conformation of mannose.

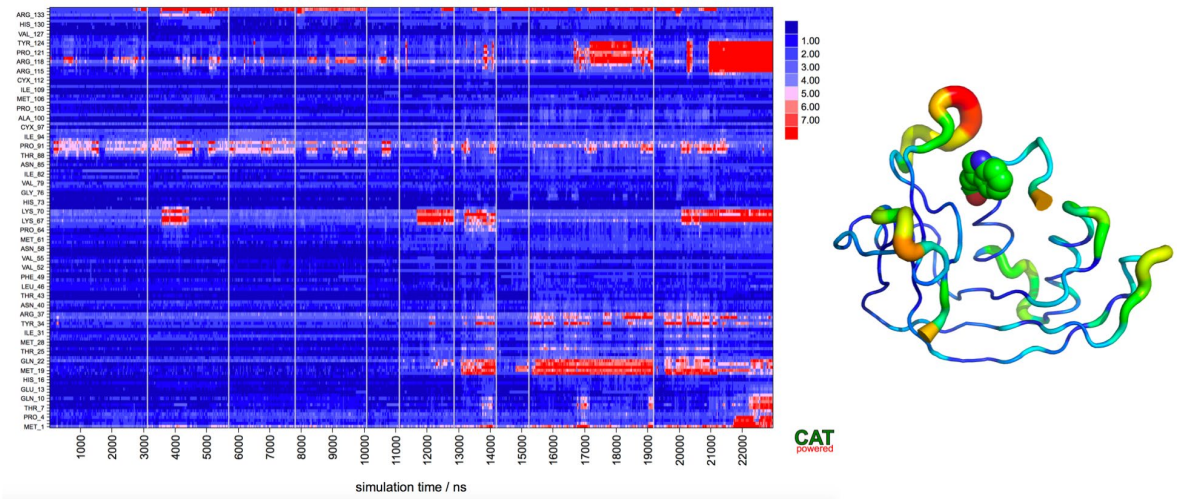

Figure S6: Stability check of RNase 2. Related to Figure 7.
Based on MD simulations in explicit solvent at 310 K (23 µs, AMBER, NPT ensemble). Left: accumulated RMSD per residue plot (individual trajectories are separated by a vertical line). Right: average residue RMSD as PyMol 'putty' representation.

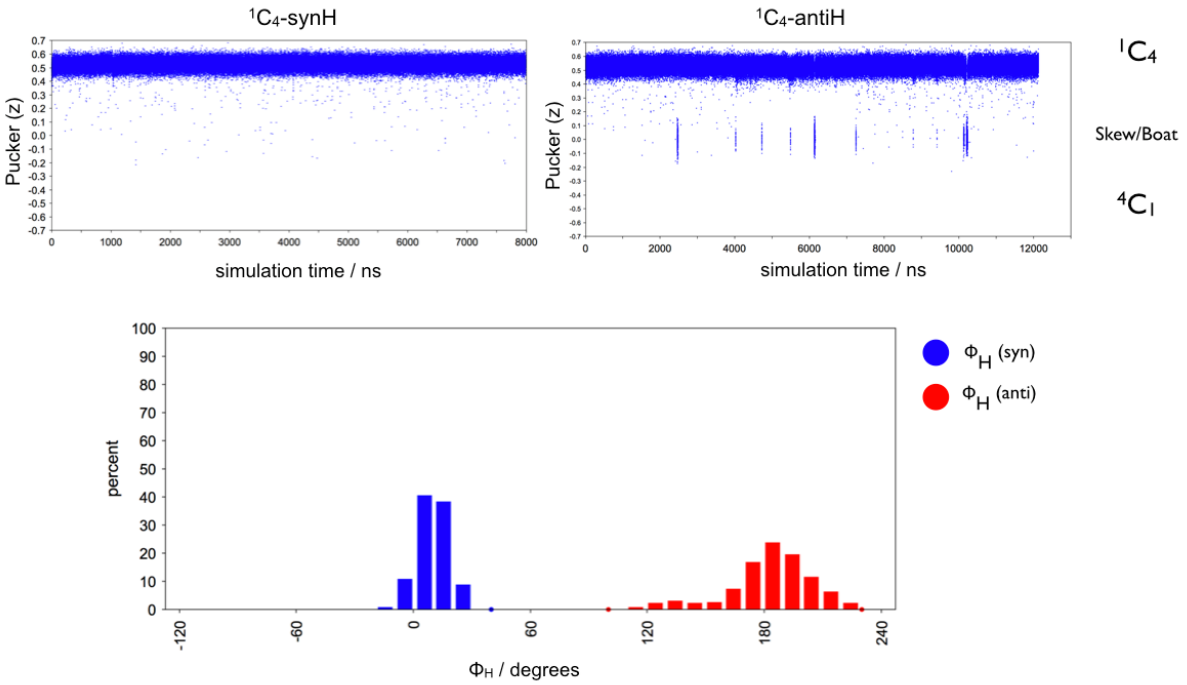

Figure S7: Stability check of ring conformations in αMan($^1C_4$)-RNase 2. Related to Figure 9.
Based on MD simulations in explicit solvent at 310 K (22 µs, AMBER, NPT ensemble). MD simulations are started with mannose in $^1C_4$-synH and $^1C_4$-antiH, respectively. It should be noted that φ_H in state antiH is more flexible and only during the simulation started from state $^1C_4$-antiH transitions to 'skew/boat' occurred.

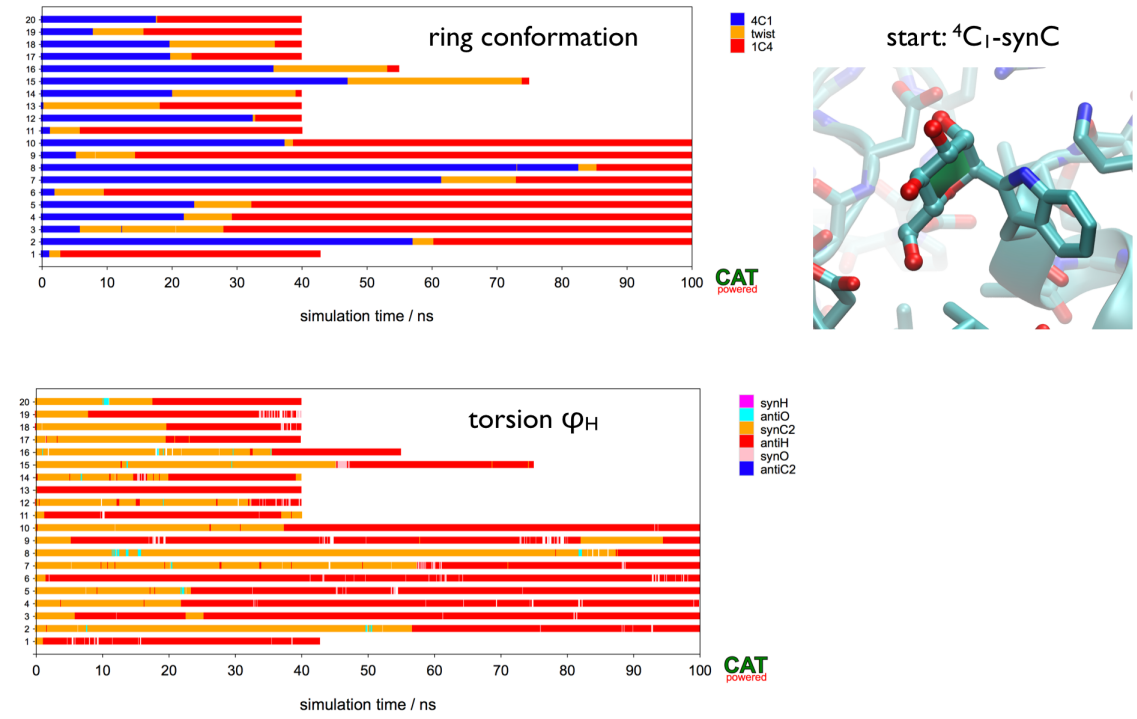

Figure S8: Stability check of αMan($^4C_1$-synC)-RNase 2.
Based on 20 MD simulations in explicit solvent at 310 K (AMBER, NPT ensemble). In all simulations a conformational transition to $^1C_4$ occurred in less than 100 ns. It should be noted that the change of the chair form is accompanied by a change of the glycosidic torsion φ_H.

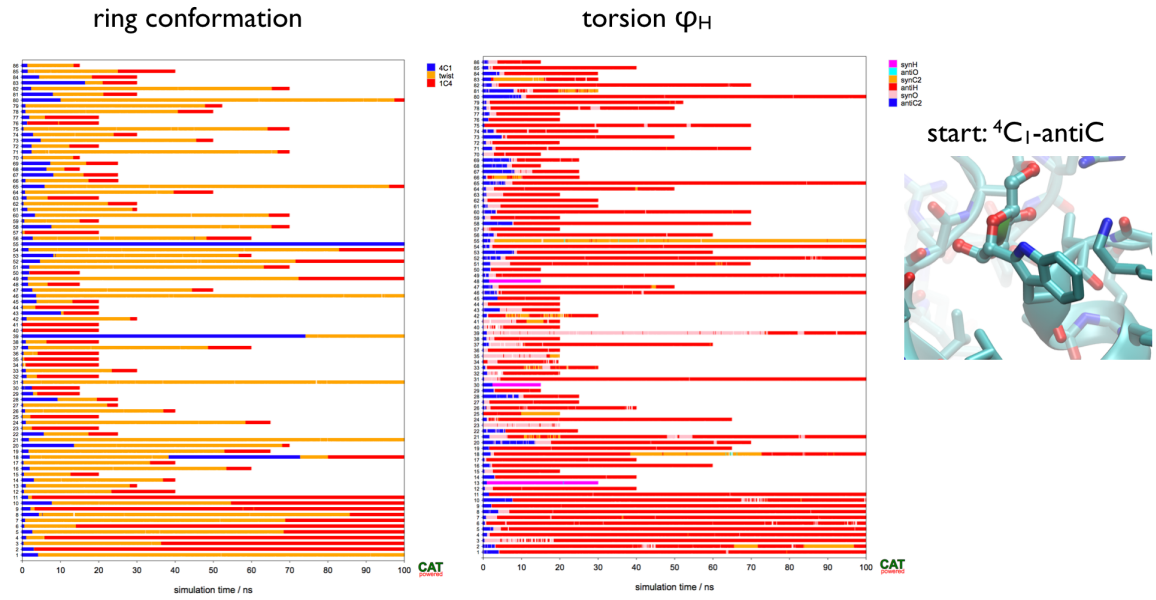

Figure S9: Stability check of αMan($^4C_1$-antiC)-RNase 2.
Based on 86 MD simulations in explicit solvent at 310 K (AMBER, NPT ensemble). It should be noted that in simulation 55 the ring form $^4C_1$ is stable for longer than 100 ns, but in this simulation φ_H has changed to synC after about 3 ns.

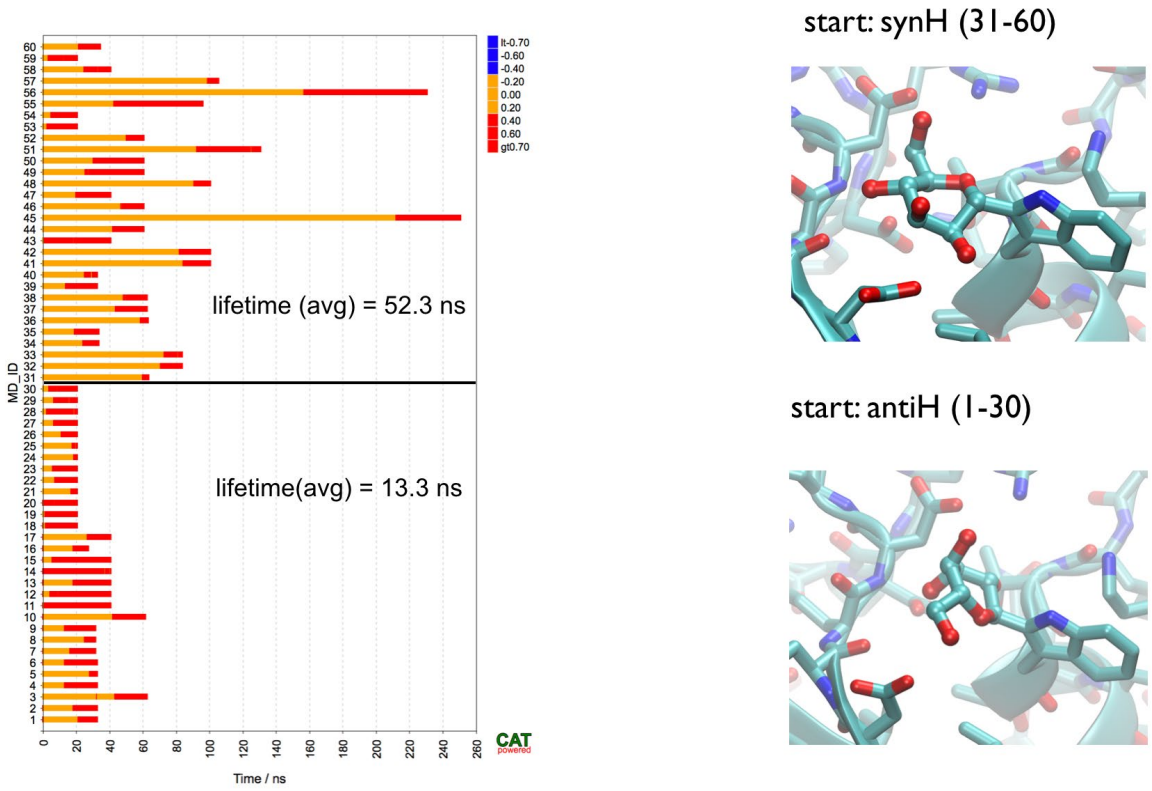

Figure S10: Stability check of αMan('skew/boat')-RNase 2.
Based on 60 MD simulations in explicit solvent at 310 K (AMBER, NPT ensemble). 'Skew/boat' have also a relatively short lifetime, however they are more stable when torsion φ_H is syn.

Supplemental Tables

Table S1: **X-rays structures of C-mannosylated proteins available in the Protein Data Bank (PDB)** (accessed 10/2019). Related to Figure 1.

Name	**PDB entries**
MAG	5lfr (2.1Å), 5lfv (2.3Å), 5lfu (4.3Å), 5lf5 (3.8Å)
Interleukin-2 Receptor	5m5e (2.3Å)
Interleukin-21 Receptor	4nzd (2.7Å), 3tgx (2.8Å)
Human Complement Component C6	3t5o (2.9Å)
Human Complement Component C8	3ojy (2.5Å)
Human Complement Component C9	6cxo (2.2Å)
C5b6	4a5w (3.5Å), 4e0s (4.2Å)
Micronemal Protein MIC2	4okr (2.6Å), 4oku (3.2Å)
ADAMTS13	3vn4 (2.8Å)
Properdin	6s08 (2.0Å), 6s0b (2.3Å), 6s0a (2.5Å), 6rus (2.8Å), 6sej (3.5Å), 6rv6 (3.5Å), 6rur (6Å), 6ruv (6.15Å)

Table S2: Experimental and calculated $J_{i,i+1}$ coupling constants.
Comparison between experimental $J_{i,i+1}$ coupling constants for the pyranose ring of Manα1-Trp from Human RNase 2 and $J_{i,i+1}$ coupling constants calculated for selected ring conformations using the generalized Karplus equation (Haasnoot et al. 1980). The following electronegativity factors were used: 1.3 for oxygen, 0.4 for carbon, 0.85 for nitrogen. Related to Table 1.

	$J_{i,i+1}$ **(Hz)**			
	H1/H2	**H2/H3**	**H3/H4**	**H4/H5**
experimental	8.2	3.2	5.3	3.4
$^{4}C_{1}$	1.4	3.2	8.0	8.5
$^{1}C_{4}$	7.7	3.1	2.8	1.2
$^{0,3}B$	3.5	3.2	2.5	3.1
$B_{0,3}$	2.8	2.9	8.1	3.7
$^{1,4}B$	7.9	6.7	8.6	8.5
$B_{1,4}$	1.3	6.7	2.2	1.1
$^{2,5}B$	1.4	3.7	1.4	1.2
$B_{2,5}$	7.7	3.1	1.8	8.5
$^{1}S_{5}$	7.7	5.4	6.0	8.3
$^{0}S_{2}$	6.7	2.1	0.8	7.2
$^{3}S_{1}$	2.3	4.4	3.4	1.6
$^{5}S_{1}$	2.0	5.2	0.9	1.5
$^{2}S_{0}$	1.4	2.2	6.6	1.9
$^{1}S_{3}$	5.4	3.8	8.9	7.2

Table S3: **Comparison between experimental ROEs contacts' intensities for the pyranose ring of Manα1-Trp from Human RNase 2 and proton distances calculated for selected ring conformations.**
Related to Table 2.

	Distances (Å)				
	H3-H5	**H1-H6**	**H4-H6**	**H2-H3**	**H1-H4**
Experimental	(ROE)W[a]	(ROE)S	(ROE)M	(ROE)S	-
$^{4}C_{1}$	2.6	4.4	2.5	2.4	4
$^{1}C_{4}$	4.4	2.4	2.6	2.4	4.0
$^{0,3}B$	3.5	4.5	2.4	2.3	4.6
$B_{0,3}$	3.2	2.5	2.5	2.4	3.4
$^{1,4}B$	2.3	3.1	2.9	2.2	1.9
$B_{1,4}$	4.2	4.1	2.5	2.2	4.8
$^{2,5}B$	4.1	2.9	2.4	2.9	4.7
$B_{2,5}$	3.3	4.5	2.5	2.4	3.2
$^{1}S_{5}$	2.7	3.8	2.7	2.3	2.3
$^{0}S_{2}$	3.7	4.6	2.4	2.4	4.1
$^{3}S_{1}$	4.2	4.4	2.4	2.3	4.7
$^{5}S_{1}$	4.2	4.1	2.7	2.3	4.8
$^{2}S_{0}$	3.5	2.6	2.4	2.5	4.0
$^{1}S_{3}$	2.7	2.3	2.4	2.3	2.4

[a] ROE intensities were estimated from cross-peak volumes in 2D-ROESY spectra recorded with a mixing time of 100 ms (De Beer et al. 1995). ROE intensities were determined as a percentage of the summed ROE and diagonal-peak intensities in a ω_2-column of the appropriate line width and were classified as weak (w, less than 5%), medium (m, 6-10%), or strong (s, more than 10%).

Table S4: Conformational preferences of C^2-α-D-mannopyranosyl-3-methyl-indole studied by quantum mechanics calculations.
GP_Energy = gas phase energy; dGP_Energy = relative gas phase energy; SP_energy = solution phase energy; dSP_energy = relative solution phase energy; Solv_energy = Solvation Energy; T-Rx: ring torsions, T_NCCO: torsion Man:O5-Man:C1-Trp:CD1-Trp:NE1. Energies are given in kcal/mol.

ID	ring_conf	Task	QM_Method	QM_Basis	GP_Energy	dGP_energy	SP_Energy	dSP_energy	Solv_Energy	T_R1	T_R2	T_R3	T_R4	T_R5	T_R6	T_NCCO
Mana_IndolMe_1C4synH-B3LYP631ssppPBF	1C4	Optimization	DFT(b3lyp)/SOLV	6-31g**++	-636253.187	5.500	-636281.187	-2.125	-27.973	46	-40	43	-55	61	-55	146.1
Mana_IndolMe_1C4synO-B3LYP631ssppPBF	1C4	Optimization	DFT(b3lyp)/SOLV	6-31g**++	-636256.000	2.687	-636283.187	-4.125	-27.184	47	-41	44	-56	61	-55	-31.5
Mana_IndolMe_1C4synO2-B3LYP631ssppPBF	1C4	Optimization	DFT(b3lyp)/SOLV	6-31g**++	-636254.000	4.687	-636279.687	-0.625	-25.623	43	-41	49	-62	62	-51	216.3
Mana_IndolMe_1C4synO_gg-B3LYP631ssppPBF	1C4	Optimization	DFT(b3lyp)/SOLV	6-31g**++	-636255.187	3.500	-636282.000	-2.937	-26.811	48	-43	44	-54	57	-52	-22.0
Mana_IndolMe_1S3synH-B3LYP631ssppPBF	1S3	Optimization	DFT(b3lyp)/SOLV	6-31g**++	-636256.437	2.250	-636278.250	0.812	-21.788	-27	67	-36	-31	74	-37	94.0
Mana_IndolMe_1S3synO-B3LYP631ssppPBF	1S3	Optimization	DFT(b3lyp)/SOLV	6-31g**++	-636257.750	0.937	-636278.812	0.250	-21.063	-23	66	-38	-29	75	-42	-86.5
Mana_IndolMe_1S3synO2-B3LYP631ssppPBF	1S3	Optimization	DFT(b3lyp)/SOLV	6-31g**++	-636256.437	2.250	-636279.312	-0.250	-22.885	-30	69	-36	-32	72	-35	94.2
Mana_IndolMe_4C1synC-B3LYP631ssppPBF	4C1	Optimization	DFT(b3lyp)/SOLV	6-31g**++	-636257.375	1.312	-636279.062	0.000	-21.702	-55	53	-48	48	-49	50	172.7
Mana_IndolMe_4C1synO-B3LYP631ssppPBF	4C1	Optimization	DFT(b3lyp)/SOLV	6-31g**++	-636258.625	0.062	-636279.812	-0.750	-21.160	-54	51	-48	53	-56	54	12.2
Mana_IndolMe_4C1synO_gt-B3LYP631ssppPBF	4C1	Optimization	DFT(b3lyp)/SOLV	6-31g**++	-636258.687	0.000	-636279.062	0.000	-20.363	-57	47	-39	46	-56	59	188.0
Mana_IndolMe_1C4synH-LMP2631ssppPBF_SP	1C4	"Single Point"	LMP2	6-31g**++	-634347.250	5.437	-634377.125	0.250	-29.918	51	-46	45	-53	59	-56	127.8
Mana_IndolMe_1C4synO-LMP2631ssppPBF_SP	1C4	"Single Point"	LMP2	6-31g**++	-634349.937	2.750	-634378.375	-1.000	-28.410	52	-46	45	-53	59	-56	-42.5
Mana_IndolMe_1C4synO2-LMP2631ssppPBF_SP	1C4	"Single Point"	LMP2	6-31g**++	-634347.437	5.250	-634374.000	3.375	-26.587	49	-45	46	-55	59	-54	187.5
Mana_IndolMe_1C4synO_gg-LMP2631ssppPBF_SP	1C4	"Single Point"	LMP2	6-31g**++	-634348.250	4.437	-634376.250	1.125	-27.983	50	-45	45	-55	59	-55	-41.8
Mana_IndolMe_1S3synH-LMP2631ssppPBF_SP	1S3	"Single Point"	LMP2	6-31g**++	-634340.937	11.750	-634372.375	5.000	-31.390	-27	67	-36	-31	74	-37	94.0
Mana_IndolMe_1S3synO-LMP2631ssppPBF_SP	1S3	"Single Point"	LMP2	6-31g**++	-634351.187	1.500	-634375.375	2.000	-24.212	-40	64	-25	-38	63	-20	-36.8
Mana_IndolMe_1S3synO2-LMP2631ssppPBF2_SP	1S3	"Single Point"	LMP2	6-31g**++	-634343.500	9.187	-634373.500	3.875	-29.986	-25	66	-38	-29	73	-40	115.2
Mana_IndolMe_1S3synO2-LMP2631ssppPBF_SP	1S3	"Single Point"	LMP2	6-31g**++	-634349.625	3.062	-634372.500	4.875	-22.872	-32	63	-28	-36	68	-30	181.1
Mana_IndolMe_4C1synC-LMP2631ssppPBF_SP	4C1	"Single Point"	LMP2	6-31g**++	-634351.375	1.312	-634376.375	1.000	-25.035	-49	52	-55	59	-56	49	238.0
Mana_IndolMe_4C1synO-LMP2631ssppPBF_SP	4C1	"Single Point"	LMP2	6-31g**++	-634352.687	0.000	-634377.375	0.000	-24.690	-52	53	-53	56	-55	51	33.9

Table S5: Hydrogen bonds between α-mannose and RNase 2 for αMan($^1C_4$-synH).
Only those with a frequency > 1% are shown. Related to Figure 10.

Index	Donor	Acceptor	Population	Distance	Angle
1	aDManp:O4	ASN_113:O	99.9	2.7	161
2	TRP_7:N	aDManp:O5	90.8	3.0	151
3	aDManp:O2	ASP_112:OD1	50.4	2.7	166
4	aDManp:O2	ASP_112:OD2	46.3	2.7	166
5	aDManp:O6	ASP_115:OD2	35.9	2.7	163
6	aDManp:O6	ASP_115:OD1	32.9	2.7	163
7	ARG_118:NH2	aDManp:O6	23.1	3.0	140

Table S6: **Hydrogen bonds between α-mannose and RNase 2 for αMan($^1C_4$-antiH)**.
Only those with a frequency > 1% are shown. Related to Figure 10.

Index	Donor	Acceptor	Population	Distance	Angle
1	TRP_7:N	aDManp:O2	55.9	3.0	150
2	aDManp:O6	ASN_113:O	46.5	2.8	154
3	aDManp:O3	ASP_115:OD1	25.0	2.7	164
4	aDManp:O3	ASP_115:OD2	17.3	2.7	164
5	aDManp:O6	ASP_112:OD1	13.9	2.7	162
6	aDManp:O6	ASP_112:OD2	12.3	2.7	162
7	aDManp:O4	ASP_112:OD1	9.0	2.7	165
8	aDManp:O3	ASP_119:OD1	8.8	2.7	163
9	aDManp:O4	ASP_112:OD2	6.8	2.7	165
10	aDManp:O6	ASP_119:OD2	5.7	2.7	166
11	aDManp:O3	ASN_113:O	5.6	2.7	158
12	aDManp:O4	ASP_115:OD2	4.4	2.7	160
13	LYS_1:NZ	aDManp:O2	3.8	3.0	133
14	aDManp:O3	ASP_119:OD2	2.7	2.9	143
15	aDManp:O4	ASP_115:OD1	1.6	2.7	162
16	ARG_118:NH2	aDManp:O3	1.3	3.0	141
17	aDManp:O6	ASP_112:O	1.1	2.9	158

Table S7: Statistics of H-H distances.
Based on MD simulations at 310 K (1 μs, AMBER, NPT ensemble) for C-glycosylated RNase 2 with αMan in $^{1}C_{4}$ ring conformation. Values are given in Å in the format "mean(stddev)[min,max]". Related to Table 1.

Distance Label	1C4(antiH)	1C4(synH)
MAN(H1-H2)	3.1(0.0)[2.9,3.2]	3.0(0.0)[2.9,3.2]
MAN(H1-H3)	3.8(0.1)[3.4,4.3]	3.8(0.1)[3.3,4.2]
MAN(H1-H4)	4.0(0.1)[3.2,4.6]	4.0(0.1)[3.4,4.5]
MAN(H1-H5)	3.8(0.1)[3.4,4.1]	3.8(0.1)[3.4,4.1]
MAN(H1-H61)	3.2(0.8)[1.7,4.7]	3.7(0.2)[1.7,4.5]
MAN(H1-H62)	2.5(0.5)[1.6,4.6]	2.2(0.2)[1.7,4.2]
MAN(H3-H5)	4.3(0.1)[3.9,4.6]	4.3(0.1)[4.0,4.5]
MAN(H4-H5)	2.6(0.1)[2.1,2.9]	2.6(0.1)[2.2,2.9]
MAN(H4-H61)	2.7(0.3)[1.9,4.0]	2.4(0.2)[1.9,3.9]
MAN(H4-H62)	3.3(0.4)[2.0,4.2]	3.1(0.2)[2.0,4.1]
MAN(H1)-TRP7(HB1)	2.1(0.1)[1.7,3.1]	3.9(0.1)[3.6,4.4]
MAN(H1)-TRP7(HB2)	3.6(0.1)[2.8,4.5]	5.1(0.1)[4.7,5.4]
MAN(H1)-TRP7(HA)	4.4(0.3)[3.3,5.4]	5.4(0.1)[4.8,6.1]
MAN(H1)-TRP7(HE1)	3.8(0.1)[3.3,4.1]	2.5(0.1)[2.0,3.0]
MAN(H2)-TRP7(HB1)	4.7(0.2)[3.5,5.4]	2.3(0.2)[1.8,3.1]
MAN(H2)-TRP7(HB2)	5.9(0.2)[4.9,6.3]	3.5(0.2)[2.6,4.3]
MAN(H2)-TRP7(HA)	5.8(0.2)[4.6,7.0]	5.1(0.2)[4.5,5.8]
MAN(H2)-TRP7(HE1)	2.6(0.2)[1.8,3.7]	4.4(0.1)[3.5,4.9]
MAN(H61)-TRP7(HE1)	6.0(0.4)[4.6,7.1]	6.0(0.3)[3.7,6.9]
MAN(H62)-TRP7(HE1)	5.5(0.2)[4.4,6.7]	4.4(0.3)[3.3,6.6]
MAN(H2)-VAL128(CG1)	7.5(0.6)[5.0,11.2]	3.7(0.6)[2.5,6.7]
MAN(H2)-VAL128(CG2)	8.6(0.6)[5.6,10.9]	4.9(0.6)[2.6,6.8]
MAN(H3)-ASP112(HB1)	9.0(0.8)[4.8,12.5]	4.4(0.4)[2.0,7.1]
MAN(H3)-ASP112(HB2)	8.1(0.9)[4.5,11.6]	3.2(0.4)[1.9,5.5]
MAN(H5)-ASP115(HB1)	7.5(1.4)[2.2,13.6]	2.2(0.2)[1.8,3.5]
MAN(H5)-ASP115(HB2)	7.8(1.0)[3.1,13.6]	3.8(0.2)[2.3,5.3]

Transparent methods

Sample purification. RNase 2 (E.C. 3.1.27.5) was a gift of J. Hofsteenge and purified from male human urine by chromatography on SP-Sephadex at pH 3.0, heparin Sepharose, and SP-Sephadex at pH 7.5. Final purification was achieved by reversed-phase HPLC, using a C4 column (Vydac, Hispania, CA) equilibrated in 0.1% trifluoroacetic acid. Protein was eluted with a linear gradient of 10.5—56% CH_3CN in 80 min, at a flow rate of 1 mL/min (Hofsteenge et al. 1994). Glycopeptides from the N-terminal region of RNase were prepared by digestion of reduced and carboxymethylated protein with the protease from *Staphylococcus aureus* (2% W/W; 18 h), thermolysin (3% W/W; 18 h), elastase (5% W/W; 4 h), or aminopeptidase M (10 units/nmol of peptide; 2h). All digestions were performed in 50 mM NH_4HCO_3, pH 7.8, at 37°C. Subsequently, glycopeptides were purified by reverse phase HPLC on a Vydac C_{18} column (4.6 X 250 mm) employing eluent A: 0.1% trifluoroacetic acid; eluent B: 0.085% trifluoroacetic acid, 70% acetonitrile. The flow rate was 1.0 ml/ min. The column was washed isocratically for 5 min with 3.5% acetonitrile after which the gradient (0.15% acetonitrile/min) was started (Hofsteenge et al. 1991).

NMR Spectroscopy. NMR spectra were recorded with a Bruker AMX-500 or AMX-600 spectrometer (Bijvoet Center, Department of NMR Spectroscopy, Utrecht University, The Netherlands), and a Varian UnityPlus 750 MHz spectrometer (SON NMR Large Scale Facility, Utrecht University). Native RNase 2 was dissolved in 90% (v/v) H_2O/D_2O, 0.1M NaCl, 1mM NaN_3, pH 5.1. NOESY and TOCSY ^{1}H-NMR spectra were recorded at 300, 315 and 320 K. 2D NOESY spectra(Jeener et al. 1979) were recorded with a mixing time of 100 ms, with 350 increments (in the t1 dimension) of 2K data points, with 96 scans per increment. Water resonance was suppressed by irradiating at low power during the relaxation delay and the mixing time. In addition, a spoil sine-bell-shaped pulsed field gradient (PFG) was applied. 2D TOCSY spectra (Griesinger et al. 1988) were recorded with a clean MLEV-17 spin lock sequence with a duration of 10, 50, or 80 ms. Spectra were recorded with 440 increments (in the t1 dimension) of 2K data points each, with 64 scans. As for NOESY experiments, water resonance was suppressed by a low power irradiation applied during the relaxation delay, and a spoil sine-bell-shaped pulsed field gradient (PFG) was included. Temperature was lowered by 3 K to avoid changes of chemical shifts due to the heat released when the sequence is applied. For all 2D experiments, quadrature detection was achieved using the State-TPPI method (Marion et al. 1989). NMR data sets were processed using NMRPipe (Delaglio et al. 1995) and TRITON NMR software packages (Bijvoet Center, University of Utrecht). REGINE software package (Bijvoet Center, University of Utrecht) was used to analyse NMR data and to perform protein assignments.
Peptides were dissolved in 5mM potassium phosphate, pH 5.4 in D_2O (99.96 atom% D, Isotec, USA). Spectra were recorded at a probe temperature of 300 K. Chemical shifts are expressed in ppm relative to internal acetone (^{1}H δ 2.225; ^{13}C δ 32.910). Suppression of the water resonance was achieved by a water eliminated Fourier Transform pulse (WEFT-pulse) sequence (Hard et al. 1992). For 1D ^{1}H-NMR spectra 16-512 free induction decays of 8K or 16K complex data points were collected. 2D spectra were acquired with 256-512 experiments of 2048 data points, with 32-240 scans per increment. Quadrature detection in the t_1 dimension was achieved by either the time-proportional phase increment (TPPI) method (Marion & Wüthrich 1983), or the States-TPPI method. 2D TOCSY experiments were recorded using a MLEV 17 mixing sequence of 20, 50 or 60 ms (Braunschweiler & Ernst 1983; Bax & Davis 1985) preceded by a trim pulse of 2.5 ms. Typically, TOCSY spectra were recorded with a mixing time of 10, 50, or 100 ms with the spin-lock field strength adjusted for a 90° pulse-length of 29-30 μs. 2D ROESY spectra were obtained with a spin-lock pulse length of 100 ms, 300 ms, 750 ms, or 1.2 s. The spin-lock field strength was in accordance with a 90° pulse of 100-120 μs. The frequency offset was initially placed on the HOD resonance and switched to about 5.7 ppm just before application of the spin-lock pulse, thereby reducing the Hartmann-Hahn transfer during the ROESY mixing time (Leeflang & Kroon-Batenburg 1992). NMR data sets were processed using ProspectND software (Bijvoet Center, University of Utrecht). Briefly, the final matrix size was zero-filled to 2Kx1K or 4Kx2K and multiplied with phase-shifted (squared-)sine-bell function prior Fourier transformation.

Molecular Modeling. The starting structures for simulations of human RNase 2 and glycopeptides were prepared based on PDB entry 1gqv (resolution 0.98 Å) using the graphical interface of YASARA (Krieger & Vriend 2014). The protonation state of amino acids was adjusted to pH 7.4 (Krieger et al. 2012). Simulations in explicit solvent (using periodic boundary conditions) were generally performed in 0.1% NaCl solution using YASARA with GPU acceleration (Krieger & Vriend 2015). Simulations at 300 K and 310 K were performed under NPT conditions. For simulations at higher temperatures the system was first equilibrated at 310 K and then the sampling was performed under NVT conditions. HTMD simulations without explicit solvent were performed with TINKER (https://dasher.wustl.edu/tinker/) using MM3 (Allinger et al. 1990). For these simulations a

dielectric constant of four was used to mimic condensed phase conditions. Conformational Analysis Tools (CAT, http://www.md-simulations.de/CAT/) was used for analysis of trajectory data, general data processing, generation of scientific plots in SVG format, and for assignment of MM3 atom types. Torsion angles are defined as φ (Man:O5-Man:C1-Trp7:CD1-Trp7:NE1), φ_H (Man:H1-Man:C1-Trp7:CD1-Trp7:NE1), χ_1 (Trp7:N-CA-CB-CG), χ_2 (Trp7:CA-CB-CG-CD1). Quantum mechanics calculations were performed with Jaguar (Version 8.1, Schrödinger, LLC). Open source Pymol (Version 1.8x, Schrödinger, LLC) and VMD (Humphrey et al. 1996) was used to generate molecular graphics.
In total more than 100 µs were sampled at various temperatures for the solvated RNase system (apo, C-mannosylated) and more than 500 µs for the glycopeptide and the model compounds (see Table below).

Overview on timescales sampled in the project

	RNASE2_apo	RNASE2_1C4	RNASE2_4C1	FTWAQW_Man	Trp_Man	Man_Indole
300 K		60 ns	4.8 µs	10 µs	3.3 µs	
310 K	23 µs	23 µs	28 µs	105 µs	116 µs	63 µs
330 K	1.1 µs	2.5 µs	3 µs	20 µs		25 µs
350K	0.5 µs	0.2 µs	0.5 µs	20 µs	2.5 µs	23 µs
370 K	3.6 µs	18 µs	10.7 µs	31 µs	5 µs	33 µs
400 K	0.3 µs	0.4 µs	0.2 µs	5 µs	17 µs	31 µs
Sum	28 µs	44 µs	47 µs	191 µs	143 µs	175 µs

In general the sampling was distributed over multiple independent simulations that were run in parallel on standard computer equipment, for example: Amber16 (PMEMD.cuda, GeForce GTX 680, RNase 2, 25713 atoms, 2 fs timestep, 66 ns/day), Gromacs 2018.2 (OPLSAA, i7-6900K CPU 3.20GHz / GeForce GTX 980, 26462 atoms, 2 fs timestep, 155 ns/day), YASARA 18.4 (AMBER03, i7-6900K CPU 3.20GHz/GeForce GTX 980, 26256 atoms, 2.5 fs timestep, 160 ns/day), YASARA 18.4 in 'fast mode' (AMBER03, i9-7920X CPU 2.90GHz/ GeForce GTX 1080 Ti, 26256 atoms, 5 fs timestep, 335 ns/day).
As can be estimated based on the example performances given for the various computer systems above, a significant amount of calculation time was consumed in the project and several Terabytes of accumulated trajectory data was output in XTC format. Individual MD simulations were typically run for at least 1 µs with a maximum of 10 µs. The distribution of the sampling over many independent simulations required the development of an efficient analysis workflow using Conformational Analysis Tools that allows to monitoring the conformational changes that are occurring in the individual simulations, and that is also able to accumulate the data of multiple MDs in order to obtain combined statistical results.

Supplemental References

Allinger, N.L., Rahman, M. & Lii, J.H., 1990. A Molecular Mechanics Force-Field (MM3) for Alcohols and Ethers. *Journal of the American Chemical Society*, 112(23), pp.8293–8307. Available at: http://pubs.acs.org/doi/abs/10.1021/ja00179a012.

Bax, A. & Davis, D.G., 1985. Practical aspects of two-dimensional transverse NOE spectroscopy. *Journal of Magnetic Resonance (1969)*, 63(1), pp.207–213.

Braunschweiler, L. & Ernst, R.R., 1983. Coherence transfer by isotropic mixing: Application to proton correlation spectroscopy. *Journal of Magnetic Resonance (1969)*, 53(3), pp.521–528.

Delaglio, F. et al., 1995. NMRPipe: a multidimensional spectral processing system based on UNIX pipes. *Journal of Biomolecular NMR*, 6(3), pp.277–293.

Griesinger, C. et al., 1988. Clean TOCSY for proton spin system identification in macromolecules. *Journal of the American Chemical Society*, 110(23), pp.7870–7872.

Haasnoot, C.A.G., de Leeuw, F.A.A.M. & Altona, C., 1980. The relationship between proton-proton NMR coupling constants and substituent electronegativities—I: An empirical generalization of the karplus equation. *Tetrahedron*, 36(19), pp.2783–2792.

Hard, K. et al., 1992. The Asn-linked carbohydrate chains of human Tamm-Horsfall glycoprotein of one male. Novel sulfated and novel N-acetylgalactosamine-containing N-linked carbohydrate chains. *European Journal of Biochemistry*, 209(3), pp.895–915.

Hofsteenge, J., Servis, C. & Stone, S.R., 1991. Studies on the interaction of ribonuclease inhibitor with pancreatic ribonuclease involving differential labeling of cysteinyl residues. *J Biochem*, 266(35), pp.24198–24204.

Humphrey, W., Dalke, A. & Schulten, K., 1996. VMD: Visual molecular dynamics. *Journal of Molecular Graphics*, 14(1), pp.33–8– 27–8.

Jeener, J. et al., 1979. Investigation of exchange processes by two-dimensional NMR spectroscopy. *The Journal of chemical physics*, 71(11), pp.4546–4553.

Krieger, E. & Vriend, G., 2015. New ways to boost molecular dynamics simulations. *Journal of Computational Chemistry*, 36(13), pp.996–1007.

Krieger, E. & Vriend, G., 2014. YASARA View—molecular graphics for all devices—from smartphones to workstations. *Bioinformatics*.

Krieger, E. et al., 2012. Assignment of protonation states in proteins and ligands: combining pKa prediction with hydrogen bonding network optimization. *Methods Mol Biol*, 819, pp.405–421.

Leeflang, B.R. & Kroon-Batenburg, L.M.J., 1992. CROSREL: Full relaxation matrix analysis for NOESY and ROESY NMR spectroscopy. *Journal of Biomolecular NMR*, 2(5), pp.495–518.

Marion, D. & Wüthrich, K., 1983. Application of phase sensitive two-dimensional correlated spectroscopy (COSY) for measurements of 1H-1H spin-spin coupling constants in proteins. *Biochem. Biophys. Res. Comm.*, 113(3), pp.967–974. Available at: http://ukpmc.ac.uk/abstract/MED/6307308.

Marion, D. et al., 1989. Rapid recording of 2D NMR spectra without phase cycling. Application to the study of hydrogen exchange in proteins. *Journal of Magnetic Resonance (1969)*, 85(2), pp.393–399.